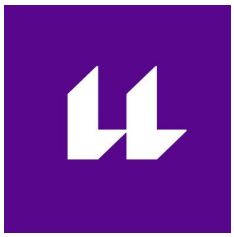

Universidad de La Laguna

Máster en Astrofísica

Characterization of star formation in nearby galaxies affected by merger events.

Memoria TFM

Author:

Diego Alfonzo Pérez Carmona

Tutor:

Helmut Dannerbauer

7^{th} September 2022

Acknowledgement

First of all, I want to thank my parents for supporting me during my career and motivating me to keep going. To my sister for listening and supporting me. To my supervisor Helmut for his advice and guidance.

Abstract

La formación estelar es uno de los parámetros más importantes en la formación y evolución de las galaxias. Las estrellas nacen principalmente en las nubes gigantes moleculares frías de las galaxias, ya que reunen las condiciones necesarias de temperatura, turbulencias y densidad, fragmentándose en regiones más pequeñas de menor masa para luego colapsar sobre ellas mismas formando estrellas.

En astrofísica se usa la tasa de formación estelar o SFR para medir el ritmo o velocidad con la que se crean estrellas en las regiones moleculares. Esta cantidad se puede obtener a partir de ciertas líneas de emisión de las nubes moleculares, provenientes de la anterior excitación de sus especies atómicas debido a la radiación de las estrellas más jóvenes y calientes, siendo las más usadas las líneas de H_α, H_β y OIII entre otras. En el trabajo de Schmidt, 1959 se descubrió que la SFR de las nubes moleculares está relacionada con la masa de estas para el caso de la Vía Láctea, y en el trabajo de Kennicutt, 1998 se aplicó (en su forma de densidad superficial) de forma global a un set de galaxias espirales normales del Universo Local (Ley de Kennicutt-Schmidt).

Sin embargo, la relación anterior obtenida por Kennicutt parece no comportarse bien para pares de galaxias interactuando entre sí. En este trabajo hemos replicado la ley de formación estelar en las regiones moleculares de 16 galaxias interactuando gravitacionalmente seleccionadas del CARMA-EDGE Survey, donde se obtienen los datos de la densidad superficial de las regiones de formación estelar a partir del flujo $J = 1 \rightarrow 0$ del $C^{12}O$ captado por la matriz combinada de radiotelescopios CARMA mientras que la densidad superficial de la SFR de dichas regiones fueron calculadas a partir de los datos del flujo de H_α procedentes de CALIFA. Con esto reproducimos la relación anterior para cada galaxia de forma individual así como para todo el conjunto de las 16 galaxias y, si bien la densidad superficial de la tasa de formación estelar o Σ_{SFR} aumenta conforme crece la densidad de gas molecular o Σ_{Mol}, tanto la pendientes n como las eficiencias de la formación estelar o SFEs obtenidas mediante el ajuste de los datos de las galaxias difieren mucho en unos casos en comparación con los resultados obtenidos en otros trabajos de la literatura, mientras que otros no tanto (incluso llegando a casi coincidir). Esto corrobora la naturaleza bimodal de la ley de formación estelar discutida en muchos trabajos anteriores y que es debida principalmente a que el medio interestelar de los pares de galaxias interactuantes sufre cambios significativos, sobre todo en las turbulencias y gradientes de velocidad presentes en él generando así regiones moleculares mucho más densas además de una caida en el valor del factor de conversión α_{CO}.

Contents

1 Introduction.

The study of the formation and evolution of galaxies covers a wide range of topics on these: from their formation through the collapse of primordial gas clouds within dark matter halos (Ellis, 1998) to their morphology, through their internal dynamics and kinematics as well, as the interaction, collision and merging between them.

One of the main mechanisms driving the evolution of galaxies is the star formation. This parameter indicates the amount of gas in the ISM (interstellar medium) of a galaxy that becomes stars and, therefore, depends on the physical properties of the galaxy.

1.1 Interstellar medium, molecular clouds and star formation.

As we know the interstellar medium (ISM) is one of the main components of galaxies. The ISM has not the same properties along the galaxy but it is formed by several regions with different physical characteristics: cold atomic gas regions (mostly HI, T = 50 - 150 K, $n_{HI} = 1 - 100 cm^{-3}$), hot atomic gas regions (mostly HI, T = 5000 - 6000 K, $n_{HI} = 0.1 - 1 cm^{-3}$), photoionized regions or HII regions (gas ionized by UV radiation from young stars, T = 5000-10000 K, $n_{HII} = 100 - 1000 cm^{-3}$) and molecular gas clouds.

It is in this last region where are the ideal conditions for star formation. In these regions (Cimatti et al., 2019), hydrogen atoms combine to form molecules of H_2 due the low temperature (T < 40K) and a column density bigger than $10^{21} cm^{-2}$. H_2 regions appear located in large molecular clouds and H_2 is the most abundant molecule. Molecular clouds have a typical temperature of about 10K. However, to maintain the gas in its molecular form, the molecules must be protected from the photons that can dissociate them. For that, the external molecules of the cloud absorb the radiation, protecting the inner molecular gas from the photodissociation.

As we said before, the hydrogen molecule is the most common molecule in these clouds but its emission is undetectable because the temperature of the molecular clouds is not enough to excite it from its rotational ground level to the next one, besides it has not a dipole moment (Glover and Low, 2011). Fortunately, the second most abundant molecule, the carbon monoxide (CO), can be detectable at typical temperature of molecular clouds. The reason why the CO is detectable and not the H_2 is because the CO has rotational emission line at low temperature, being very useful to subtract information about molecular clouds because its rotational transition lines ($J = 1 - 0$ and $J = 2 - 1$) are produced by a low transition energy with a temperature smaller than the average temperature of molecular clouds.

1.2 Interacting galaxies and mergers

The interaction between galaxies is a fundamental pillar in the galaxy formation and evolution scheme. In the Λ CDM model, the interacting galaxies and mergers throughout the time affect the Star Formation History (SFH), AGN activity and galaxy structure between others aspects (Jogee et al., 2009). It is very common to use simulations to study the effects of interacting galaxies in their evolution. For example, in the simulation made by Rupke et al. (2010) they found that the metallicity gradient drop due to merger-driven inflow of poor metallicity gas from the the progenitor disk of interacting spiral galaxies (see also Torrey et al. (2012)).

This interaction occurs when 2 (or more) galaxies are too close of each other. Their gravitational fields start to "drag" the stars, dust and gas of the galaxies to the system mass central, making gas and stellar tidal bridges connecting both galaxies, modifying the morphology and structure of these galaxies. Sometimes, the interaction between 2 or more galaxies ends up in a merger building a single galaxy in the process, where the gas of the galaxy experiments shock heated, cooling and compression (Cimatti et al., 2019), influencing on some properties like SFR and metallicity (Hwang et al., 2011).

Figure 1: *Image of the NGC 7764A group of galaxies interacting with each other took by the Advanced Camera for Surveys (ACS) and the the Wide Field Camera 3 (WFC3) installed on the Hubble Space Telescope (credits: https://www.mdscc.nasa.gov/index.php/2022/01/31/hubble-detecta-un-par-galactico-en-forma-de-nave-estelar/)*

1.3 Star formation

The star formation is one of the main mechanism that rules the galactic formation and evolution. In fact, it is the first step of the formation of galaxies: the primordial cold gas into dark matter halos collapse itself to form the first stars that will build-up the galaxies (Cimatti et al., 2019). In fact, to form the first stars this primordial gas must be in molecular form, such as H_2, HD, and LiH (Puy and Signore, 1999) and be in low temperature and high density. But low temperature and relatively high density are not enough to molecular clouds collapse. Others important physical processes must be included in the star formation, like the magnetic field, the density profile and the velocity structure or turbulence (Bergin and Tafalla, 2007). But it seems that density profile and turbulence are the most important factor. In the simulations made in Girichidis et al. (2011), they found that the density profile of a molecular cloud could affect the star formation in it: if the density profile is $\rho \propto r^{-1.5}$, the molecular cloud is too sensible to turbulence, driving it to collapse in an unique massive star or in many low-mass stars, but if $\rho \propto r^{-2}$, there will only be a massive core and the turbulence has not influence over it. On the other hand, the turbulence has an important role in the regulation of the star formation (Krumholz and McKee, 2005; Evans, 1999).

One can measure the star formation activity of a molecular cloud, galaxy or set of galaxies using the star formation rate, which is the mass of gas collapsing to form stars divided by the free-fall time (Krumholz and McKee, 2005). The surface density of this quantity can be related with the gas surface density in the form of a power law called the Schmidt-Kennicutt Law. In (Schmidt,1959) this law was discovered using the volumen density of molecular clouds from the Milky Way, but in the extragalactic scheme, it was derived using the surface density of 61 normal spiral galaxies and related it with the SFR surface density (Kennicutt Jr, 1998). Mathematically is expressed as:

$$\Sigma_{SFR} = A\Sigma_{mol}^{N} \tag{1}$$

Where Σ_{mol} is the molecular surface density Σ_{SFR} is the SFR surface density ad A is the SFR efficiency coefficient (Kennicutt Jr, 1998). This power-law depends on the exponent N which depends on the trace used, like H_α flux (very strong in star formation regions due the presence of young massive stars). Others tracers can be useful to measure the SFR like the lines [OI], [OIII] and [CI] (De Looze et al., 2014).

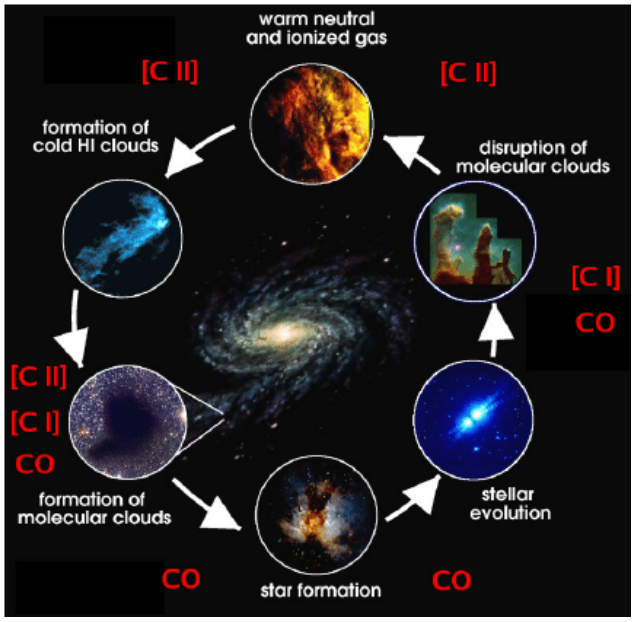

Figure 2: *Diagram of the star formation cicle (credits: https://www.researchgate.net/figure/Sketch-of-the-various-stages-in-the-life-cycle-of-interstellar-clouds_fig1_258788364.*

1.4 Motivation and objective.

The aim of this thesis is characterize the correlation between molecular gas and SFR surface density (Kennicutt-Schmidt relation) of a subsample of a few galaxies in merger events from the EDGE and CALIFA surveys and to compare it with others results from the literature. From this comparison we will know if the gravitational interaction between pairs of galaxies and merging galaxies lead to a significant change on the star formation in this galaxies due to the perturbations on the turbulence of molecular clouds.

2 Surveys and telescopes

2.1 CALIFA

CALIFA (Calar Alto Legacy Integral Field Area) is a Integral Field Spectroscopy (IFS) survey of about 600 galaxies in the nearby Universe. The sample of galaxies were observed with the Postdam Multi-Aperture Spectrophotometer PMAS (Roth et al., 2005) instrument installed on the 3.5 metres Telescope in Calar Alto (Almeria, Spain) and using the wide integral field unit PPak (Kelz et al., 2006), thus allowing to obtain the spectra of each pixel that are arranged into a datacube of the field of view (3D spectroscopy).

The aim of this survey is to create 2D maps of the age and metallicity of stellar population; distribution, chemical abundances and excitation mechanism; and the kinematic properties

of ionized gas and stellar components, using the PPAK Integral Field of View (IFU) with a FOV of 1.3″ (Sánchez et al., 2012). The wavelength range is from 3700 to 7000 Å, using the V500 and V1200 settings with a resolution of R 850 and R 1650, respectively.

The first sample of CALIFA, also called Mother Sample, was selected following the criteria presented in (Walcher et al., 2014): i) All objects were selected from the SDSS DR7, specifically the ones that have an isophote major axis at 25 mag per square arcsecond in the r band between 45″ and 79.2″. ii) excluding the Galactic plane ($b > 20^{o}$ or $b <$ -20^{o}) and impose an upper magnitud limit of 20 in the r band to avoid photometric problems. iii) The redshift range chosen is 0.005 4 $< z <$ 0.03 in order to discard stars and the objects that do not appear in SIMBAD nor SDSS. iv) Limitating the hour angle between 2h and -2h and the declination angle to $\delta > 7^{o}$ (this limit is applied only for a Right Ascension between 5h and 20h).

The Mother Sample has over 900 galaxies but this amount was reduced to a subset of about 667 galaxies (DR3), selecting those that have a $M_b < -18$ in addition to cover a large range of physical galaxy properties (Sánchez et al., 2012). From the 667 galaxies of the DR3, 646 targets have data cubes in the V500 configuration and 484 in the V1200 configuration and each datacube has about 1000 independent spectra, thus in total this DR comprises 400,000 total independent spectra. CALIFA is a legacy survey, intended for the community. For all this, CALIFA is an important resource for archaeological studies of galaxies in the Local Universe.

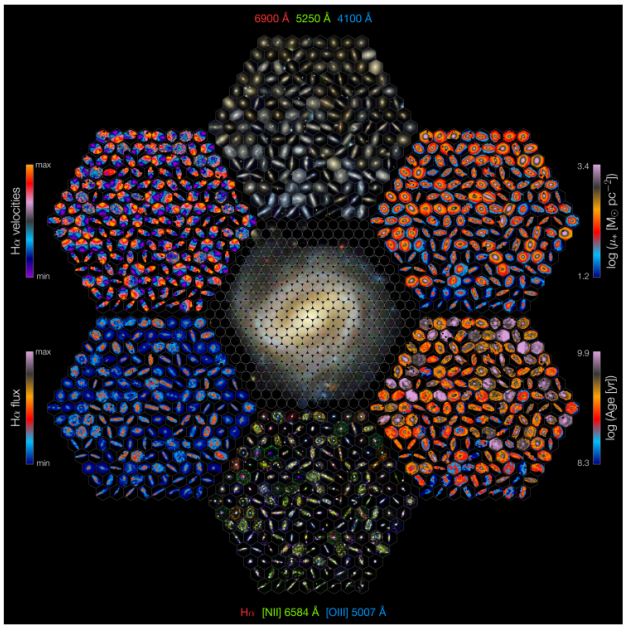

Figure 3: *Image of the NGC 7764A group of galaxies interacting with each other took by the Advanced Camera for Surveys (ACS) and the the Wide Field Camera 3 (WFC3) installed on the Hubble Space Telescope (credits: https://www.mdscc.nasa.gov/index.php/2022/01/31/hubble-detecta-un-par-galactico-en-forma-de-nave-estelar/)*

2.2 CARMA

To carry out research in various field of astrophysics, scientists use the technique of millimeter interferometry in observations: from the planetary atmospheres of the solar system to the structure of the universe on a large scale (Woody et al., 2004). The Combined Array for Research in Millimeter Wave Astronomy (CARMA) was a collaboration between five institutions with the goal of improving the sensitivity, image quality, and frequency coverage for millimeter wave interferometry.CARMA was an astronomical interferometer being the combination of Owens Valley Millimeter Array and BIMA Millimeter Array (Pound et al., 2001).

The array consists of six 10.4-m from OVRO, nine 6.1-m telescopes from BINA and eight 3.5-m telescopes from SZA. OVRO and BINA telescopes have 4 configurations (A, B, C, D) with baselines of 7 m to 2 km, getting images with an angular scale from 30" to 0.1" at 1 mm (Beasley and Vogel, 2003), and in addition of the SZA telescopes, CARMA gets images with an angular scale greater tha 0.1". Also, CARMA operated in two bands: 3-mm band (84-116 GHz) and 1-mm band (215-270 GHz). Both bands coverage most of the importants molecular lines emission, like CO, SiO, HCN, etc.

One of the dominant components that determines the sensitivity of millimeter interfer-

ometry has been atmospheric opacity (Woody et al., 2004). Operating at a higher place, CARMA has a considerable in its scientific capacity, combining more telescopes of multiple sizes, using an updated correlator as well as a new data pipelin computer system among others. CARMA is located in Cedar Flat at an approximated altitude of about 2.2km where the annual median zenith opacity of 225 GHz is 0.25 nepers, having the 50% of OVRO one at an altitude of 1,200 m. allowed observations at 1.3 mm during most of the time (Woody et al., 2004).

During the years that CARMA was operative, it has provided many type of useful astrophysical data: the detection of CO emission lines from numerous objects at low and high redshift can be useful to understand the formation and evolution of galaxies and stars.

Figure 4: *Image of the OVRO and Bima, forming the radio-observatory CARMA.*

2.3 EDGE survey.

The CARMA-EDGE (Extragalactic Database for Galaxy Evolution) survey (Bolatto et al., 2017) is the CO $J = 1 - 0$ interferometric database of 126 bright infrarred galaxies with a strong correlation between IR and CO luminosity selected from CALIFA survey taken them by CARMA interferometer , making it the largest galactic ^{12}CO and ^{13}CO survey in the local universe. Originally, the sample consisted in 177 galaxies with a high $22\mu m$ flux emission observed by WISE and mostly located around 12 hours of right ascension. This first set of galaxies were observed in the E configuration of CARMA, sampling of with 40 minutes of integration per galaxy. Each target was observed with a seven-point hexagonal mosaic for the most galaxies, producing a half-power field of view with a radius of 50". But from the original set of 177 galaxies, a group of 126 galaxies were observed with the D configuration, during 3.5 hours of integration for each target with a seven-point hexagonal mosaic for all the sub-sample.

The observation mode of CARMA used in the campaign was snapshot: the targets were observed following a priority order which consists on the highest priority target being the closest to a given elevation and integration time need. Each galaxy and a near phase-referencing

quasar were observed. Furthermore, for a better switching target, the sample was divided in 3 groups based in their redshifts (1500-4000 km/s, 4000-6500 km/s and 6500-9000 km/s). Futhermore, the correlator has been configurated in 2 frequency windows: 5 windows of 250 MHz encompassing the ^{12}CO emission line with a resolution of 3.4 km/s and a velocity range of 3000 km/s and 2 windows of 500 MHz for the ^{13}CO emission line with a resolution of 14.3 km/s and a velocity range of 3800 km/s.

To calibrate the data they used MIRIAD (Multi-Channel Imaging Reconstruction, Images, Analysis, and Display) via the pipeline from scripts for the STING galaxy survey. To determine the passband gains, a quasar of bright < 8 Jy was observed (3C273 or OJ 287), and for the flux calibration were observed Mars, Uranus, MWC349 H II region and quasar 3C273, with a systematic uncertainty in the flux calibration scale of about $\pm 10\%$.

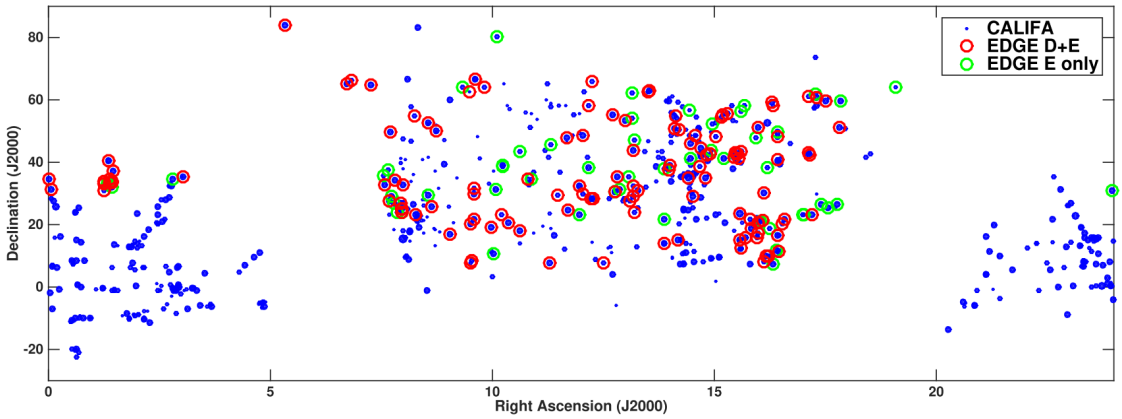

Figure 5: *Localization of the galaxies from EDGE and CALIFA surveys on the sky. In filled blue points are the galaxies from CALIFA. The size of these points represents the logarithm of the SFR corrected from H_α extinction. The red circle represent the galaxies from EDGE observed using the E+D CARMA configuration. And the green ones are the EDGE galaxies observed using only the D CARMA configuration (Bolatto et al., 2017)*

3 Interacting galaxies sample.

3.1 Sample selection

The sample chosen for this thesis consists in a group of 16 interacting and mergered galaxies from the 126 galaxies of EDGE-CARMA Survey (Bolatto et al., 2017).

To select our sample of interacting and merged galaxies, we need to focus on their morphological properties. So, to identify the evolutionary stage of interacting galaxies, we use the classification methodology presented in Bridge et al. (2010):

- Galaxies with long tidal tail. A fundamental characteristic of intermediate and late stage of merging galaxies process.

- Galaxies with medium tidal tail, which size is similar to the size of host galaxy.

- Galaxies with tidal tail shorter than the diameter of the host galaxy. This presents many problems in the interaction/fusion of spiral and barred galaxies because of the tidal tail can be mistaken for one of the spiral arms.

- Galaxies with tidal bridge linking to another galaxies. This phase occurs after the first encounter between galaxies in the merging process.

- Galaxies with double nuclei.

The next table summaries the characteristics of the merging galaxies sample from CARMA-EDGE with data from NASA/IPAC:

Name	RA	DEC	Hubble dist. (Mpc)	Redshift	Diameter (kpc)	Description	TIR Luminosity (10^{10} $L_\odot$)
NGC0523	01h25m20.73s	+34d01m29.84s	66.09 +/- 4.64	0.01588	58.25	Tidal bridge tail	4.08
NGC2480	07h57m10.44s	+23d46m47.31s	37.60 +/- 2.64	0.00782	17.62	Short tidal tail	-
NGC2623	08h38m24.07s	+25d45m16.70s	85.39 +/- 5.98	0.01851	58.37	Long tidal bridge tail	35.2 (LIRG)
UGC05108	09h35m26.29s	+29d48m45.38s	123.96 +/- 8.68	0.02714	70.62	Short tidal tail	6.55
NGC3303	10h36m59.80s	+18d08m12.0s	97.53 +/- 6.84	0.02095	89.28	tidal bridge tail	-
NGC4211	12h15m36.6s	+28d10m25s	101.53 +/- 7.12	0.02199	61.24	Medium tidal tail	2.89
NGC4676A	12h46m10.11s	+30d43m54.90s	100.61 +/- 7.05	0.02186	69.94	Long tidal tail	-
UGC08107	12h59m39.78s	+53d20m28.20s	124.68 +/- 8.73	0.02766	97.26	?	5.98
NGC5218	13h32m10.38s	+62d46m03.91s	43.42 +/- 3.04	0.00949	30.87	Tidal bridge tail	3.90
NGC5394	13h58m33.65s	+37d27m12.55s	97.68 +/- 6.84	0.02187	62.55	Short tidal tail	5.63
NGC5614	14h24m07.59s	+34d51m31.86s	59.99 +/- 4.20	0.01298	29.18	?	2.52
NGC5930	15h26m07.94s	+41d40m33.82s	40.20 +/- 2.82	0.00878	21.43	Tidal bridge tail	4.01
NGC5934	15h28m12.77s	+42d55m47.73s	83.34 +/- 5.83	0.01856	48.72	Long tidal tail	3.38
NGC5953	15h34m32.38s	+15d11m37.59s	30.97 +/- 2.17	0.00656	15.74	Medium tidal tail	2.62
ARP220	15h34m57.25s	+23d30m11.30s	83.13 +/- 5.82	0.01840	52.65	Tidal bridge tail	106.34 (ULIRG)
UGC10205	16h06m40.18s	+30d05m56.70s	97.68 +/- 6.84	0.02187	62.55	Short tidal tail	2.17

Table 1: Characteristics parameters of galaxies sample from CARMA-EDGE and NASA/IPAC. Last column tell us the reason to identify each galaxy as interacting/merging galaxy. The last column shows the TIR (total infrarred) luminosity (in 10^{10} $L_\odot$ from Catalán-Torrecilla et al. (2015). Only 2 galaxies have a infrarred luminosity $> 10^{10}$ $L_\odot$, specifically NGC 2623 ($> 10^{11}$ $L_\odot$) is a LIRG and ARP 220 ($> 10^{12}$ $L_\odot$) is a ULIRG.

In Table 1 we show the principal parameters of our galaxy sample, such as their distance, redshift, diameter, RA and Dec. positions from NASA/IPAC database. Also, we added another column that describes shortly the visual characteristics of each galaxy that indicates us the reason why it is an interacting or merging galaxy. Finally, the last column shows the TIR luminosity (in 10^{10} $L_\odot$) of each galaxy, standing out the cases of NGC 2623 (LIRG) and ARP 220 (ULIRG).

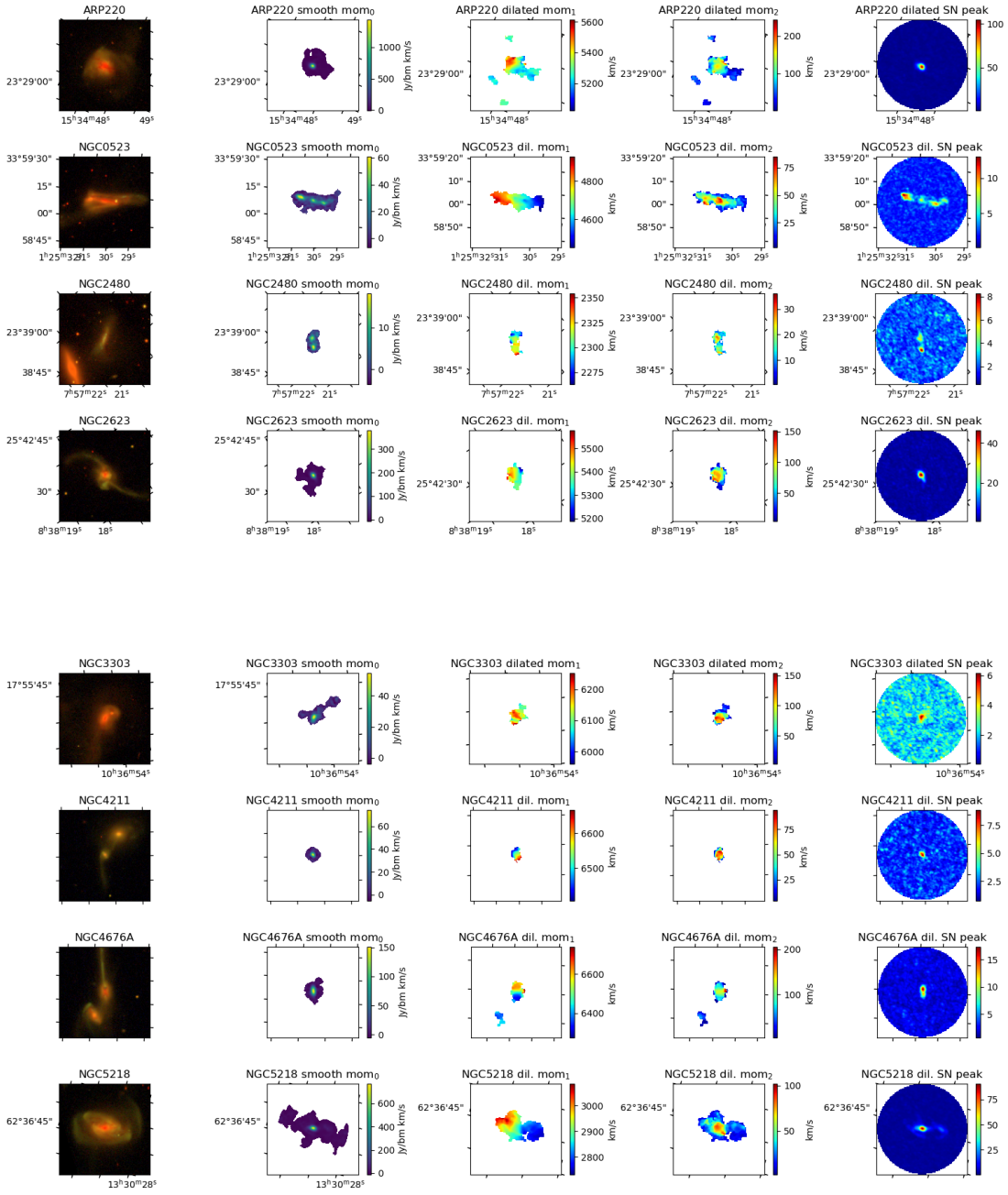

Figure 6: *Mergered/interacting galaxies selected from EDGE survey. The first images column is a SDSS DR12 RGB composition of each galaxy. The second images column is the smoothed CO zero moment flux in Jy/bm km/s. The third column is the dilated CO first moment in km/s. The fourth column is the dilated CO second moment in km/s. And the last column is the signal-noise relation peak of each galaxy.*

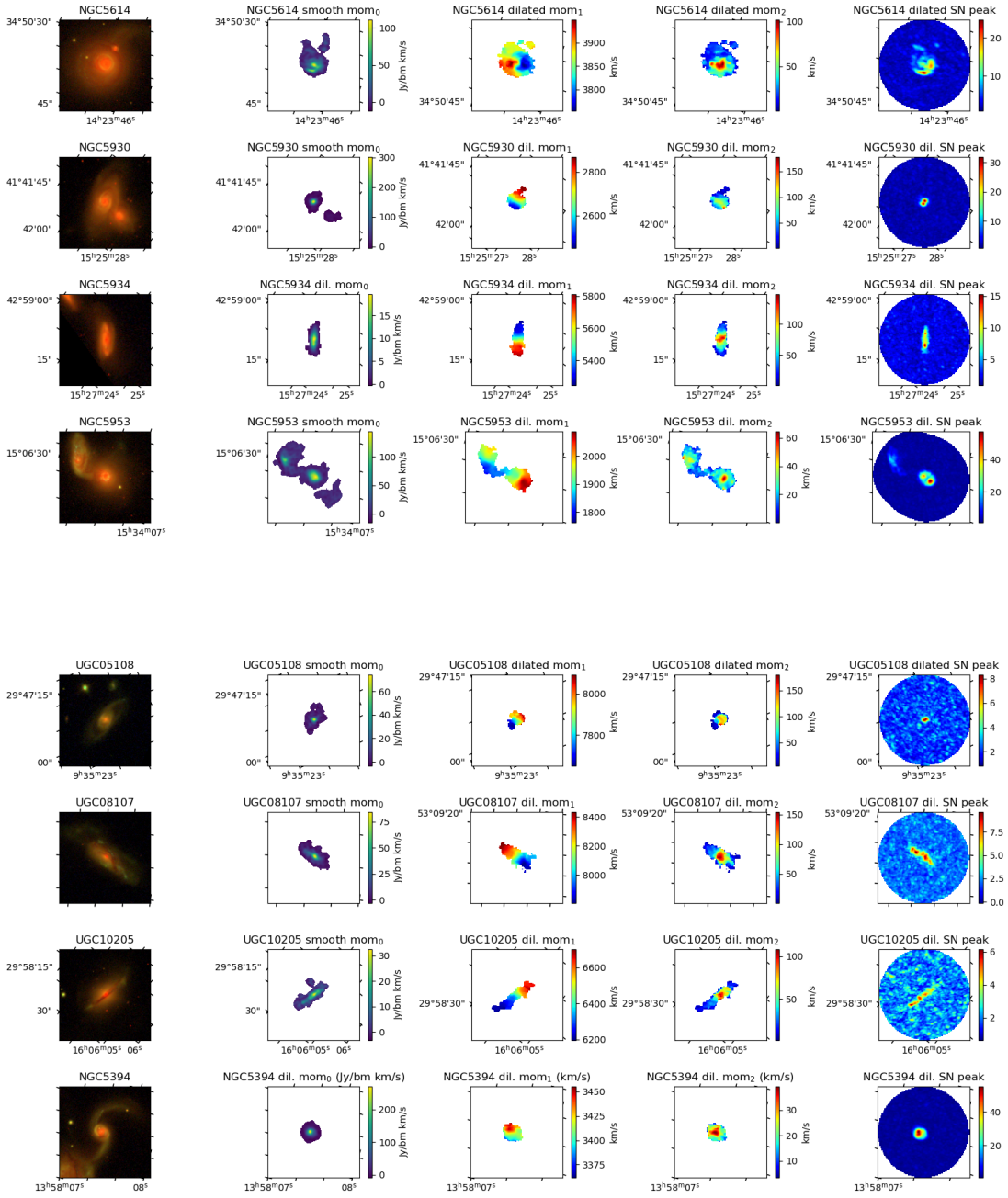

Figure 6: *Continuation*

In Figure 6 we show our galaxy sample from EDGE and CALIFA surveys. The first column we have made a RGB composition using the g, u and r band images of each galaxy from the SDSS DR12. In the second column we plot their respective smoothed moment zero

of the CO J=1-0 emission line. At the same time, the 2 next columns show their dilated moment 1 and 2 maps respectively. And finally, we have signal-to-noise peak map of each galaxy. The smoothed moment zero map was obtained by convolving to a resolution of 14" (cite) the image of the CO J=1-0 emission line of the galaxies. While, the dilated moments 1 and 2 were obtained using peaks $\geq 3.5\sigma$ on the smoothed datacube and spreading it to a 2σ contour (Bolatto et al., 2017) for the line of sight velocity and velocity dispersion respectively.

3.2 Database and Python EDGE Tool

To bring about the data analysis we use the EDGE Python Database developed by Tony Wong. Here we discribe briefly the characteristics of the Python Database from T. Wong et. al 2022 (in preparation).

The CARMA-EDGE and CALIFA data is divided in 3 type of files or tables: 0-dimensional table (a single value for each galaxy), 1-dimensional table and higher dimensional tables.

To handle the data, they wrote a Python class code, based on the astropy.table.Table class, called EdgeTable. This allows, among others things, transfer a data column from a table to another one as well as plot them. To work with the CARMA-EDGE and CALIFA data, one must to install the Python edge_pydb package (see https://github.com/tonywong94/edge_pydb).

The 0-dimensional tables are CSV files that content observational characteristics (integration time, integrated line flux of CO and HI,...) as well as those obtained by the CALIFA team (SFR, stellar mass, metallicity,...) and by the team EDGE. The 1-dimensional tables, also in CSV format, contain the radial profile and spectra data. Finally, the higher dimensional tables (images), in HDF5 format, can be divided in 3 subgroups:

-The 2-dimensional tables ('[label].2d_smo7.hdf5') have the CO moment maps data taken by CARMA with a resolution of 7". These maps are matching in resolution with the CALIFA data. At the same time, the CO moment maps were obtained using 3 methods: straight mask (no mask was applied and have a low signal-to-nois ratio), smoothed mask and dilated mask (both were explain in the previous subsection). Each moment map type is separated from the others by paths within the HDF5 file. To work the CO moment map with straight, smoothed or dilated mask, is necessary to indicate their paths using the keywords 'str', 'smo' and 'dil' respectively. Also, the CALIFA data are in another path ('ELINES_sm').

-The 3-dimensional tables ('[label].pipe3d.hdf5') have the CALIFA data divided in 5 different paths: 'ELINES', 'SFH', 'SSP', 'flux_elines' and indices, which 'ELINES' and 'flux_elines' provide the SFR, metallicity, age data,...

-Others 2-dimensional tables ('[label].cocube_smo7.hdf5') have the CARMA CO datacube and mask cubes, at a resolution of 7 arcsec (FWHM Gaussian beam).

Working with allpix Pipe3d file

In [3]:
```
sspcols = ['Name','ix','iy','mass_ssp','sigstar']
fluxcols = ['Name','ix','iy','flux_Halpha','flux_Hbeta','e_flux_Halpha','e_flux_Hbeta',
            'flux_sigsfr0','flux_sigsfr_corr','flux_sigsfr_adopt','EW_Halpha']
comomcols = ['Name','ix','iy','mom0_12','e_mom0_12','sigmol']

# Read the tables
#globaltab = EdgeTable('edge_califa.csv', cols=['Name','caMass'])
#cofluxtab = EdgeTable('edge_coflux_smo7.csv', cols=['Name','coNomaskDv_smo7','coSmoothDv_smo7'])
fluxtab = EdgeTable('edge_carma_allpix_082021.pipe3d.hdf5', path='flux_elines', cols=fluxcols)
ssptab = EdgeTable('edge_carma_allpix_082021.pipe3d.hdf5', path='SSP', cols=sspcols)
#cotab = EdgeTable('edge_aca_allpix.pipe3d.hdf5', path='comom_dil', cols=comomcols)
#conomasktab = EdgeTable('edge_aca_allpix.pipe3d.hdf5', path='comom_str', cols=['Name','ix','iy','e_mom0_12'])
print('Working on full EDGE database')
```

```
Working on full EDGE database
```

In [4]:
```
# consolidate the tables
fluxtab.join(ssptab)
#fluxtab.join(cotab)

print(fluxtab.colnames)
```

```
['Name', 'ix', 'iy', 'flux_Halpha', 'flux_Hbeta', 'e_flux_Halpha', 'e_flux_Hbeta', 'flux_sigsfr0', 'flux_sigsfr_corr', 'flux_si
gsfr_adopt', 'EW_Halpha', 'mass_ssp', 'sigstar']
```

Figure 7: *Fragment of the CARMA-EDGE Python Datacode implemented.*

4 Results

4.1 Data selection

For the purpose of this work, we have used the EDGE Python Database (Figure 7) which has different types of data of galaxies belonging to the CARMA-EDGE Survey and we have processed them with the edge_pydb python package. Most of the data is from a HDF5 file named 'carma_edge_allpix.2d_smo7.hdf5', which has the CO flux, H_α flux, stellar mass surface density and others. In the Python code, following the tutorial in https://github.com/tonywong94/edge_pydb, we opened the data file using the "EdgeTable" class. This HDF5 file contains other files/tables (named "paths") in which are the data from CALIFA and EDGE. Also, in the parameter "cols" we write the name of the data columns that we have needed. The tables we need for this work are called 'flux_elines_sm', which has data flux of the galaxies from CALIFA, with the columns 'Name' (name of the galaxy), 'flux_Halpha_sm' (H_α flux), 'e_flux_Halpha_sm' (H_α flux error), 'flux_sigsfr_uncor_sm' (Σ_{SFR} uncorrected from H_α extinction), 'flux_sigsfr_cor_sm' (Σ_{SFR} corrected from H_α extinction) and 'flux_sigsfr_adopt_sm' (Σ_{SFR} corrected from reduced noise H_α extinction) and 'comom_dil' (dilated CO mask data) with the columns 'Name', 'mom0_12' (CO flux), 'e_mom0_12' (CO flux error) and 'sigmol' (molecular gas surface density) (T.Wong et al. 2022 -in prep.-). Then we unified the columns

selected before in a single table and create a subtable with all the data corresponding to H_α and CO fluxes $> 3\sigma$ and finally choose the data of the merger galaxy sample.

4.2 Galaxy sample

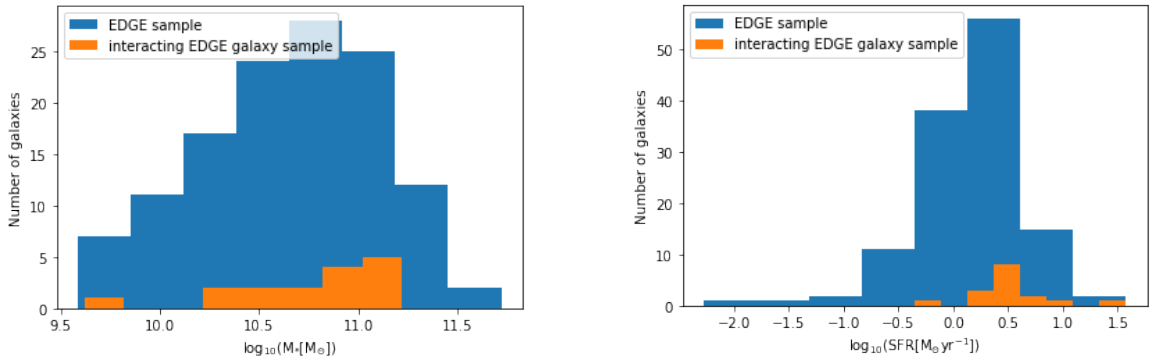

Figure 8: *Comparison between the distribution of galaxy parameters in our galaxy merger sample from CARMA-EDGE and the whole sample of this one. The left graphic represents the distribution of galaxies by their total stellar mass and the right one represents the distribution of galaxies by their SFR (in $M_\odot\ yr^{-1}$ of both samples.*

The Figure 8 represents the distribution of the galaxies by their stellar mass (left graphic) and SFR (right graphic) of our galaxy merger sample from CARMA-EDGE and the whole galaxy sample from this survey (Bolatto et al., 2017). We can see that most our merger galaxies are massive. Also, most of them have high SFR ($> 1\ M_\odot yr^{-1}$) and the distribution of the number of galaxies respect to their SFR is quiet similar to the EDGE sample.

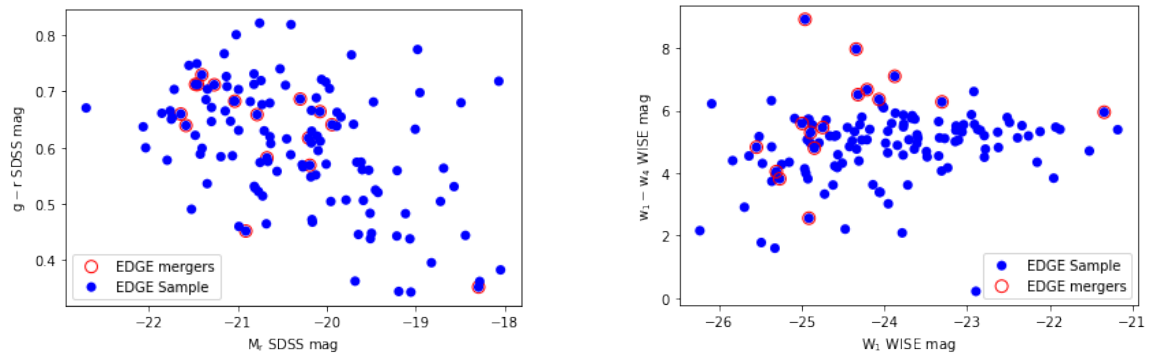

Figure 9: *Position of our merger galaxy sample in color-magnitude spaces in the context of the whole CARMA-EDGE sample. The left panel shows the location of our galaxies (red rings) and CARMA-EDGE galaxies (blue filled circles) in the SDSS color-magnitude space. The right panel shows the location of our galaxies (red rings) and CARMA-EDGE galaxies (blue filled circles) in the WISE color-magnitude space.*

The left panel of Figure 9 shows the distributions of the galaxies in the SDSS color-magnitude space (optical). Most of them span in the $0.55 < g - r < 0.75$ and have an

absolute magnitude $M_r < -20$ (except one galaxy). The right panel, instead, shows the distributions of the galaxies in the WISE color-magnitude space, in the infrared region of the spectrum. The y-axis is the $3.4\mu m - 22\mu m$ flux ratio and the x-axis is the absolute $3.4\mu m$ magnitude, which correspond to the specific star formation rate and stellar mass (Bolatto et al., 2017).

4.3 Maps

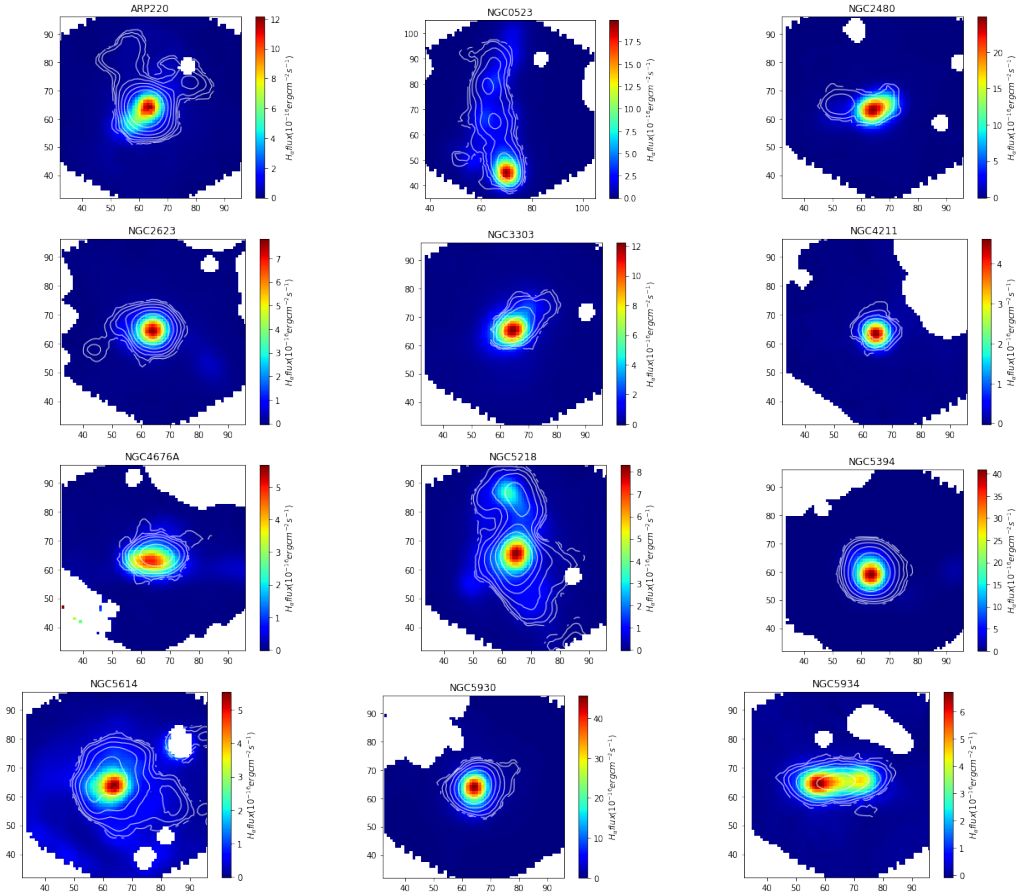

Figure 10: *H_α flux maps in $10^{-16} erg\ cm^{-2} s^{-1}$ of the merger sample with 1, 2.2, 4.6, 10, 22, 46, 100 CO flux contours in units of $K\ km/s$.*

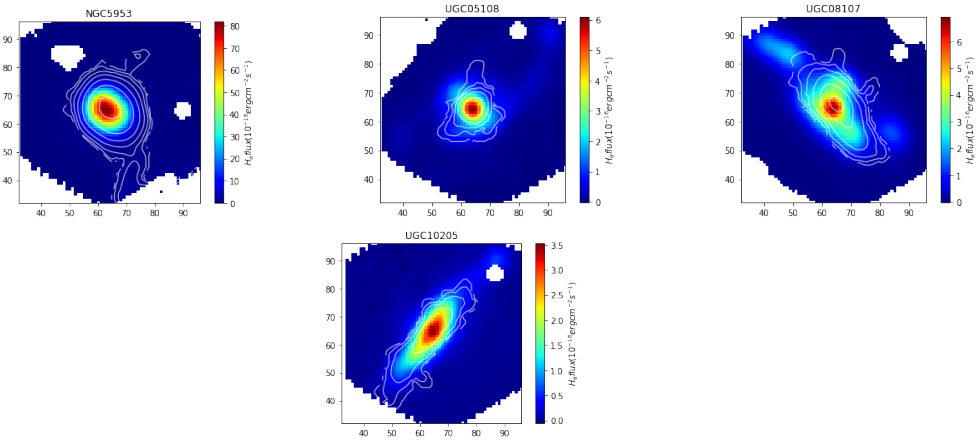

Figure 10: *Continuation*

In Figure 10 we show the H_α flux maps (in $10^{-16} erg\ cm^{-2} s^{-1}$ with CO flux level contours (from the outermost to the innermost) of 1, 2.2, 4.6, 10, 22, 46 and 100 in units of $K\ km/s$ overlapped of each galaxy. We can see that the innermost contours (the ones which delimit the areas with the highest CO lux emission) surround the brightest H_α of the galaxies. This was to be expected because in giant molecular clouds, some of the born stars are massive stars that emit enough energetic photons to dissociate and ionize the surrounding gas. This gas expands far away from the massive stars (typically O and B type stars) inside the giant molecular clouds. These zones are HII regions in which one of the most important emission line is the H_α and is very useful to study star formation nebulae and the star formation rate as a calibrator (Hopkins et al., 2001; Rosa-González et al., 2002). On the other hand, we used CO flux to make contours to show us the size and sections of the molecular clouds because the $J = 1 - 0$ CO emission line is a good H_2 tracer. In previous work it was discovered that there is a linear relation between the H_2 column density to the integrated CO emission line expressed as (Bolatto et al., 2013):

$$N_{H_2} = X_{CO} I_{CO} \tag{2}$$

Where N_{H_2} is the column density of H_2 in cm^{-2}, I_{CO} is the integrated CO emission line in $K\ km\ s^{-1}$ and the X_{CO} factor in $cm^{-2}/K\ km\ s^{-1}$. This equation is equivalent to the molecular mass-CO luminosity relation (Bolatto et al., 2013):

$$M_{mol} = \alpha_{CO} L_{CO} \tag{3}$$

As we can see in Equation 2 and Equation 3 the molecular mass (assuming that $M_{mol} = M_{H_2}$ is directly proportional to CO luminosity.

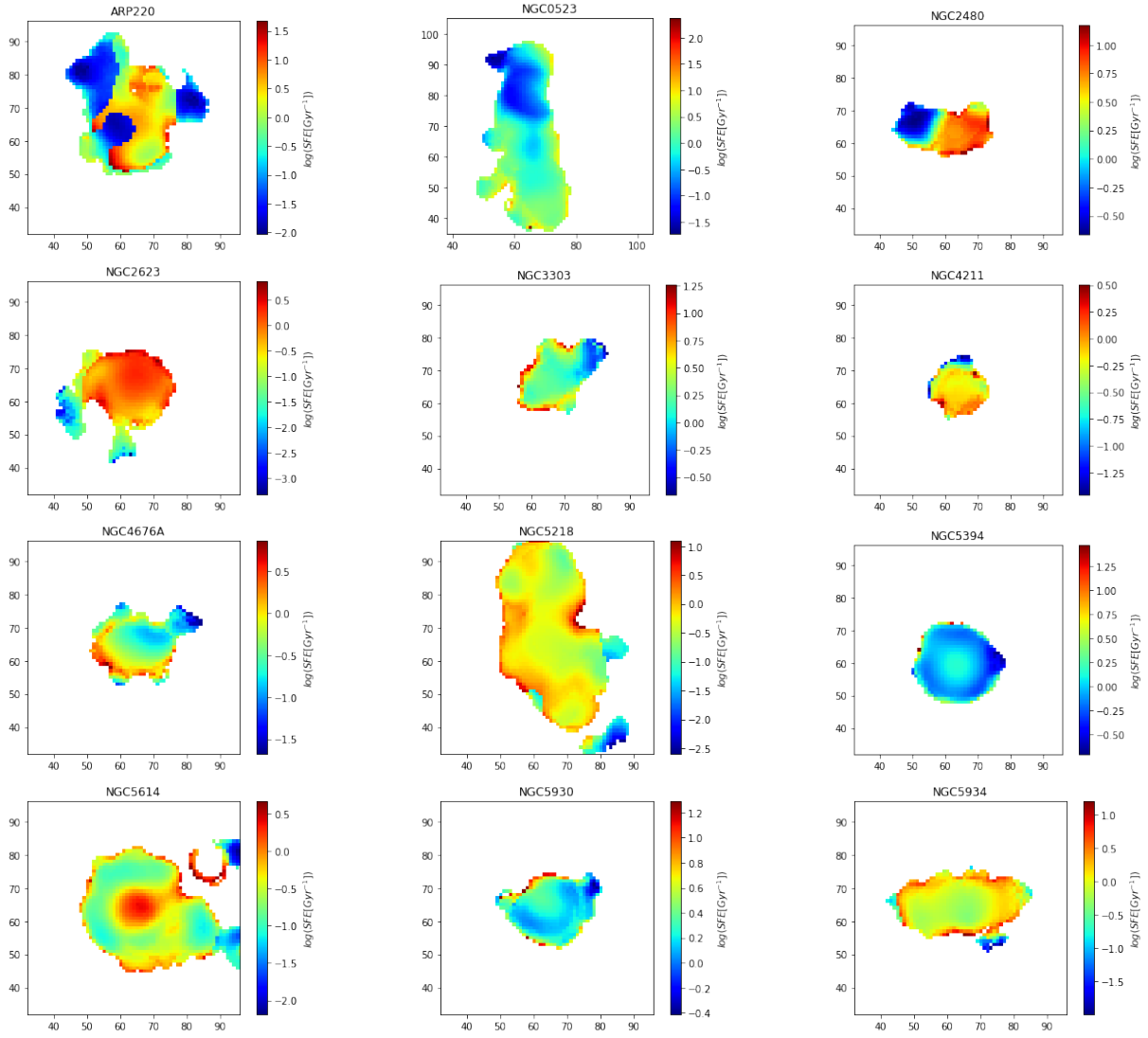

Figure 11: *Logarithmic Σ_{SFR}-Σ_{mol} relation maps of the each galaxy of the sample. For each map we have used the Σ_{mol} values from the dilated CO mask and the Σ_{SFR} adaptable from CALIFA.*

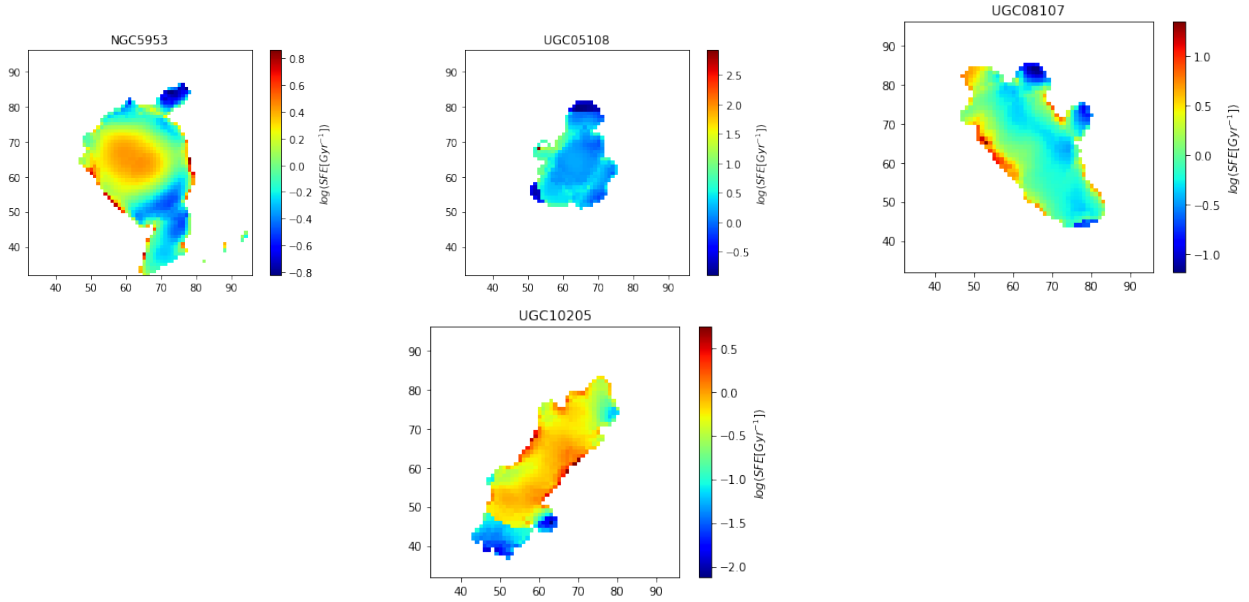

Figure 11: *Continuation.*

In Figure 11 we have the Σ_{SFR} vs Σ_{mol} maps of the sample. The magnitud shown in these maps is the logarithmic reason of Σ_{SFR} vs Σ_{mol}:

$$log_{10}(\frac{\Sigma_{SFR}}{\Sigma_{mol}}) \tag{4}$$

This quantity is the logarithmic star formation efficiency or SFE and is the inverse of the depletion time (know as consumption time). The depletion time (τ_{depl}) is the time spent by the star formation to consume the gas of a galaxy with the current SFR (Cimatti et al., 2019) and that means larger SFE values imply shorter τ_{depl} and viceversa. We can see some galaxies from the sample having regions with high SFE values, for example NGC 2623, NGC 4211, NGC 5934 and NGC 5614. Therefore, galaxies as ARP 220, NGC 0523, and NGC 2480 have a strong dependence in their SFEs with its position: the SFE is larger when it is near the brightest H_α region (Figure 10), as well as in NGC 2623, NGC 4211, NGC 5614, NGC 5930, NGC 5953, UGC05108 and UGC 10205. On the other hand, the high SFE regions of the rest of the sample (Figure 11) do not coincide with the brightness H_α regions (Figure 10). In Equation 1 the constant A is the SFE and it can reach typical large values in some galaxies, which have a high star formation rate compared with the average SFR in most galaxies also called starburst galaxies. The increment of the SFR in these galaxies is usually triggered by the interaction between 2 or more galaxies (Conselice et al., 2000; Joseph and Wright, 1985; Knapen and Cisternas, 2015), Joseph and Wright (1985) because the gas from the molecular clouds of those galaxies experiences shocks that increasing its density on those regions, implying in an enhancement of the SFR (Dopita et al., 2002).

4.4 Star formation law and scaling relations

4.4.1 Star formation law

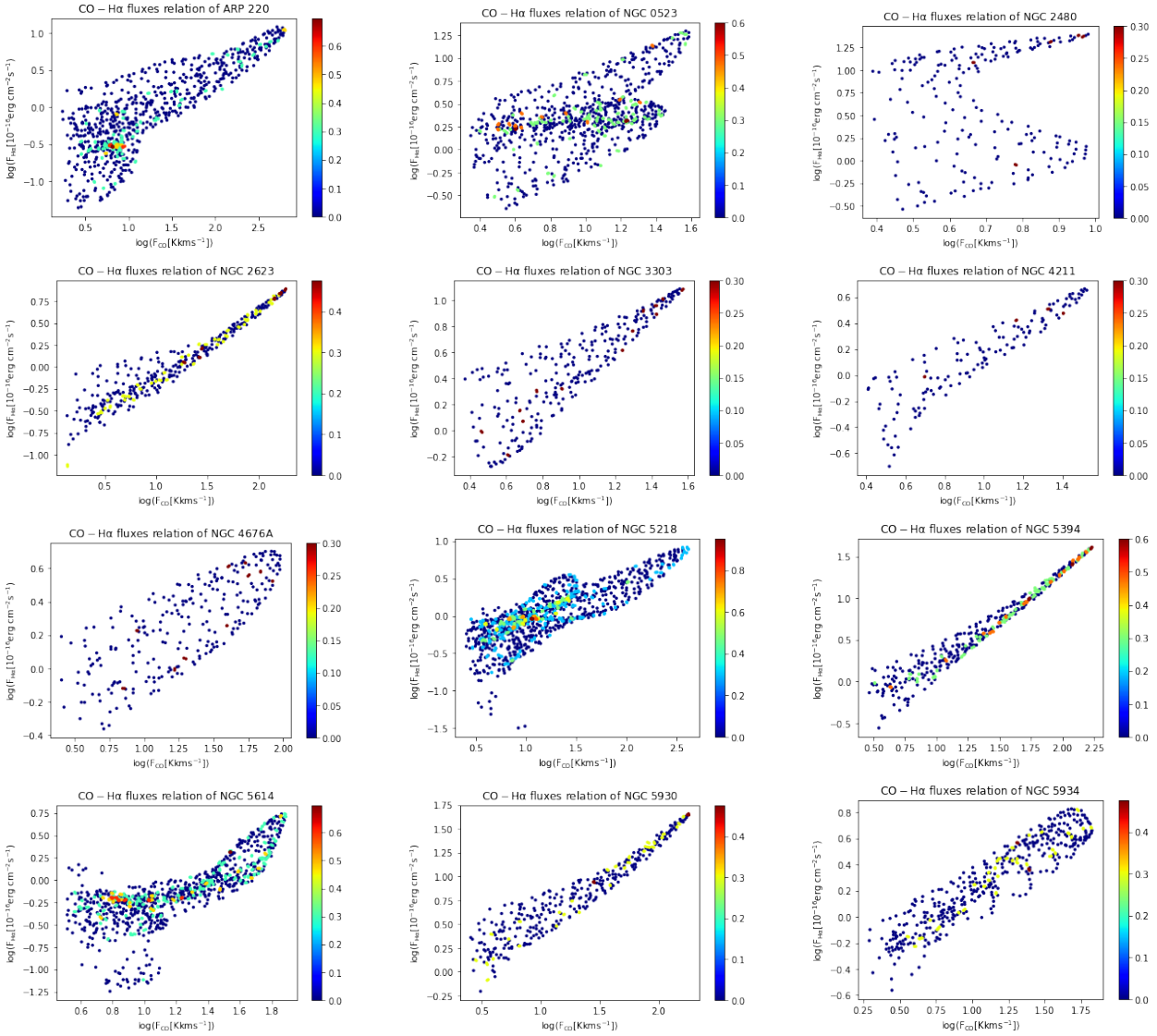

Figure 12: *Logarithmic H_α vs CO flux relation of each galaxy from our merger sample. In the y-axis it is represented the $logH_\alpha$ and in the x-axis it is represented the $logCO$. The units of H_α and CO flux are $10^{-16} erg\ cm^{-2}\ s^{-1}$ and $K\ km\ s^{-1}$ respectively. The color gradients indicate the number of independent data points with similar values.*

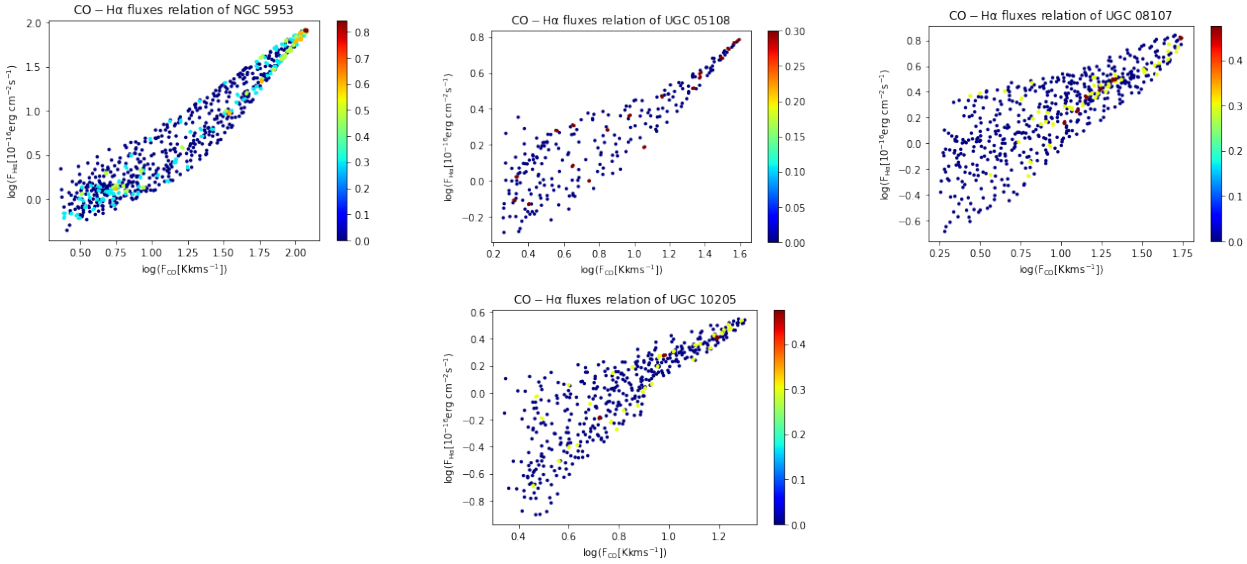

Figure 12: *Continuation.*

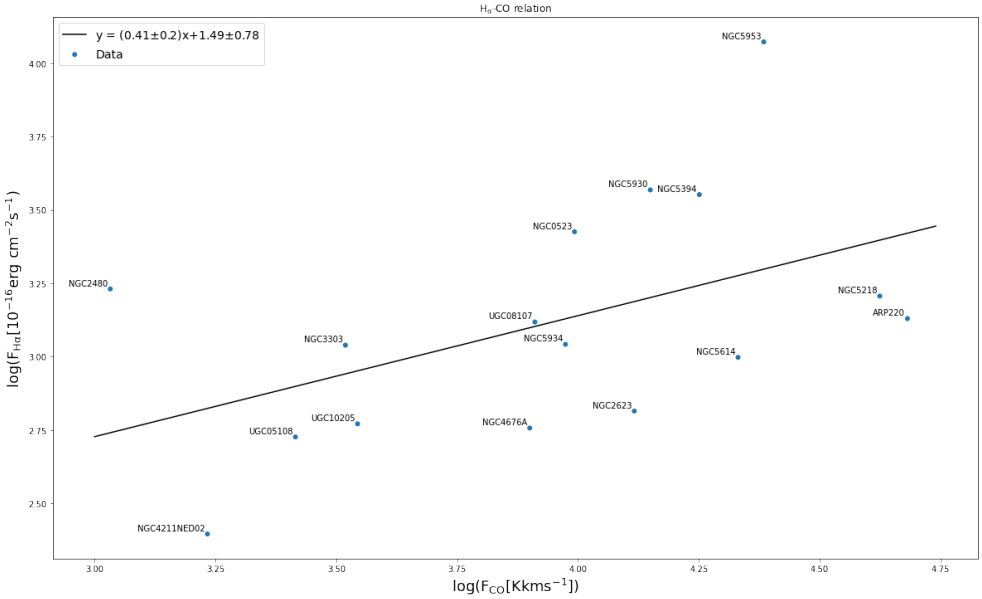

Figure 13: *Logarithmic H_α vs CO flux integrated of the sample. In the y-axis it is represented the logH_α and in the x-axis it is represented the logCO. The units of H_α and CO flux are $10^{-16} erg\ cm^{-2}\ s^{-1}$ and $K\ km\ s^{-1}$ respectively. The black line is the best fit of the relation using the data plotted here.*

In Figure 12 is represented the logarithmic relation between H_α flux and CO flux of each galaxy from our merger sample. We can see that there is a linear relation between both magnitudes in their logarithmic form. However, in the graphics corresponding to the galaxies

NGC 0523 and NGC 2480 2 branches can be seen, indicating that in those galaxies there massive molecular clouds with high and low H_α luminosity.

In Figure 13 (which represents the H_α vs CO flux integrated of the sample) we can see that H_α flux emission increases with the CO flux emission. However, galaxies like NGC 5953 emit high H_α flux and others like NGC 4211 emit low H_α flux.

We know that, from Equation 2 and Equation 3, the mass of a molecular region is directly proportional to CO luminosity. This relation is a different way to see the star formation law since the SFR of a molecular cloud can be calculated by its H_α flux (Rosa-González et al., 2002) and its mass by its CO flux (Bolatto et al., 2013).

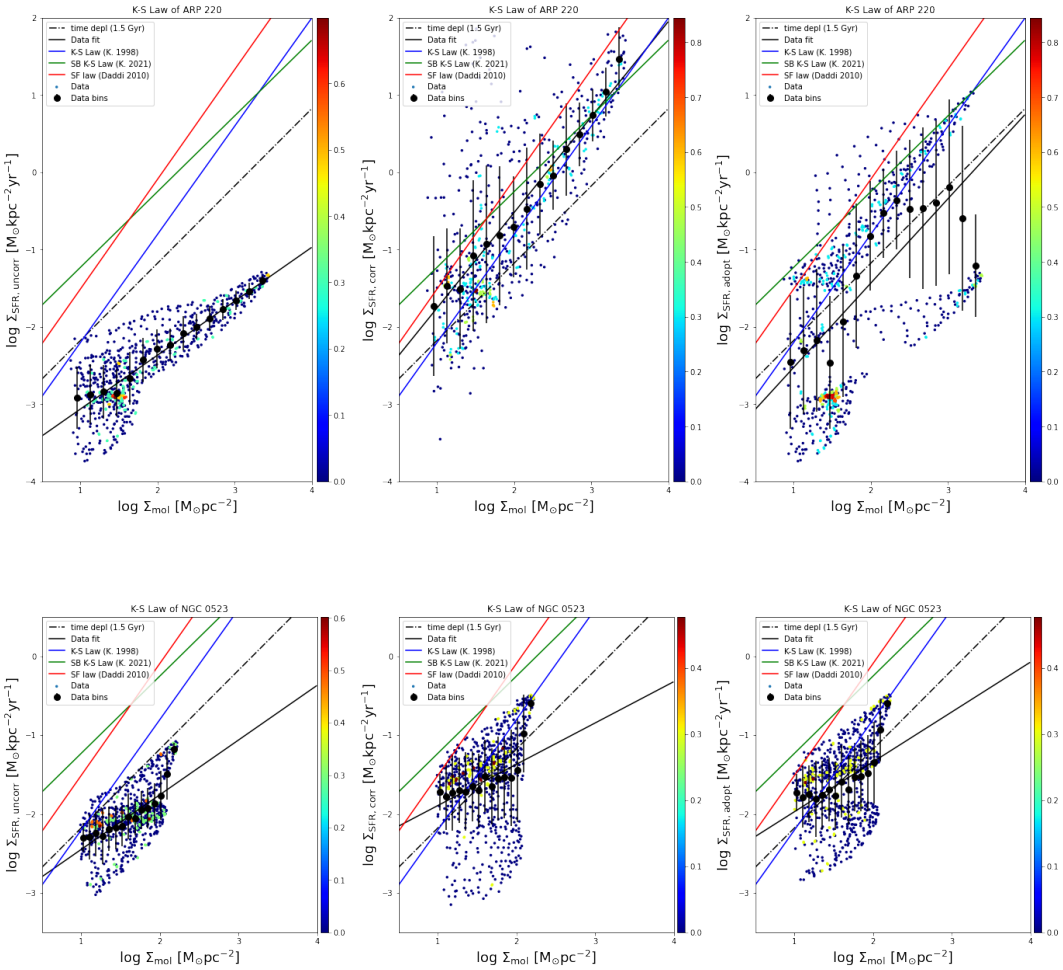

Figure 14: *Logarithmic Σ_{SFR}-Σ_{mol} relation, as known as Star Formation Law, of each galaxy from the sample. Each dataset is divided by 15 bins, where the black filled points are the average values of $log_{10}\Sigma_{mol}$ and $log_{10}\Sigma_{SFR}$ of each bin. The black line is the best fit of the datasets, while the blue line is the best fit for normal spiral galxies from Kennicutt Jr (1998) and the green one is the is the best fir for starburst galaxies from Kennicutt and De Los Reyes (2021). The dash-point line indicates the time depletion of about 1.5 Gyr. The color gradients indicate the number of independent data points with similar values.*

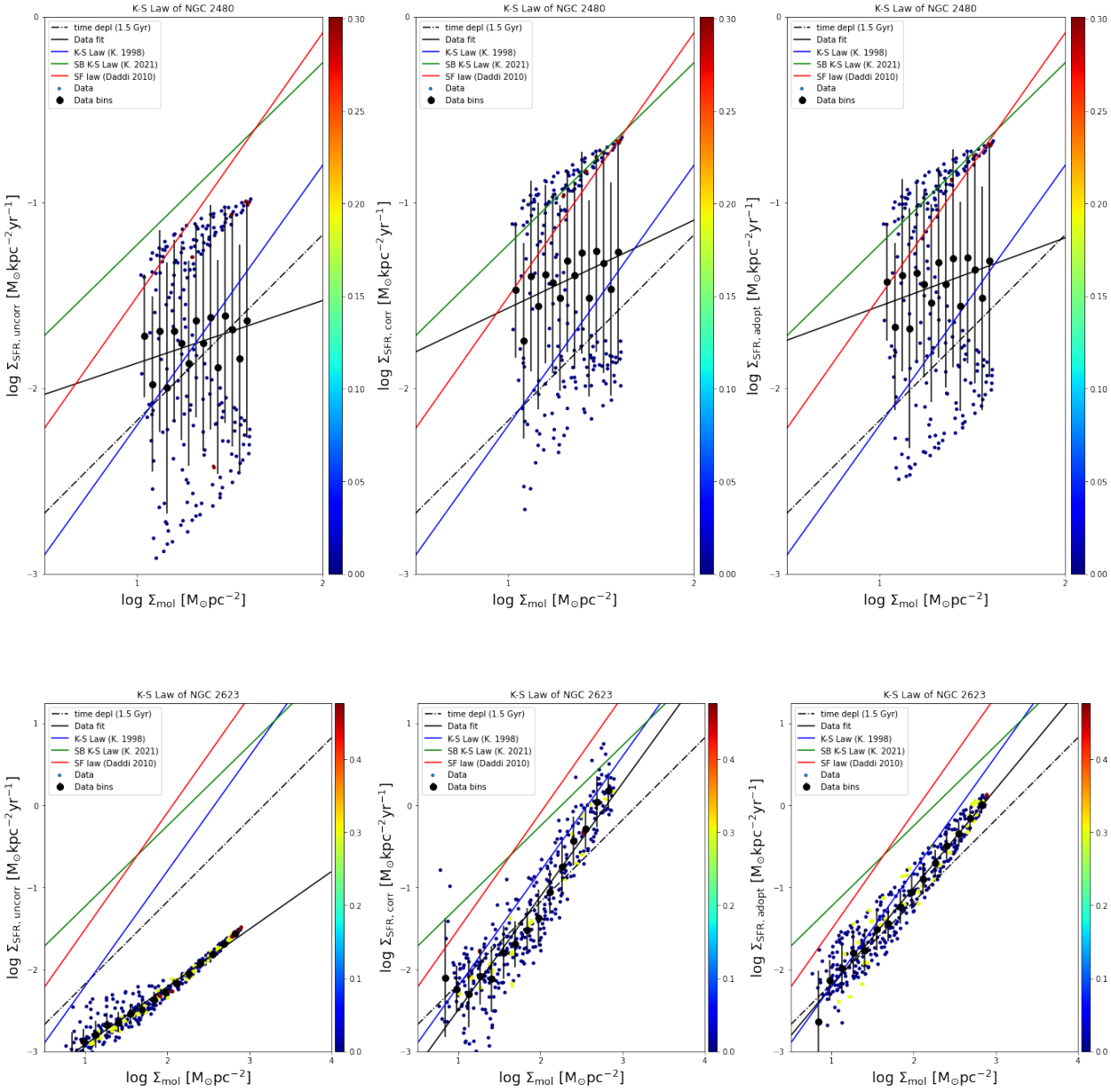

Figure 14: *Continuation*

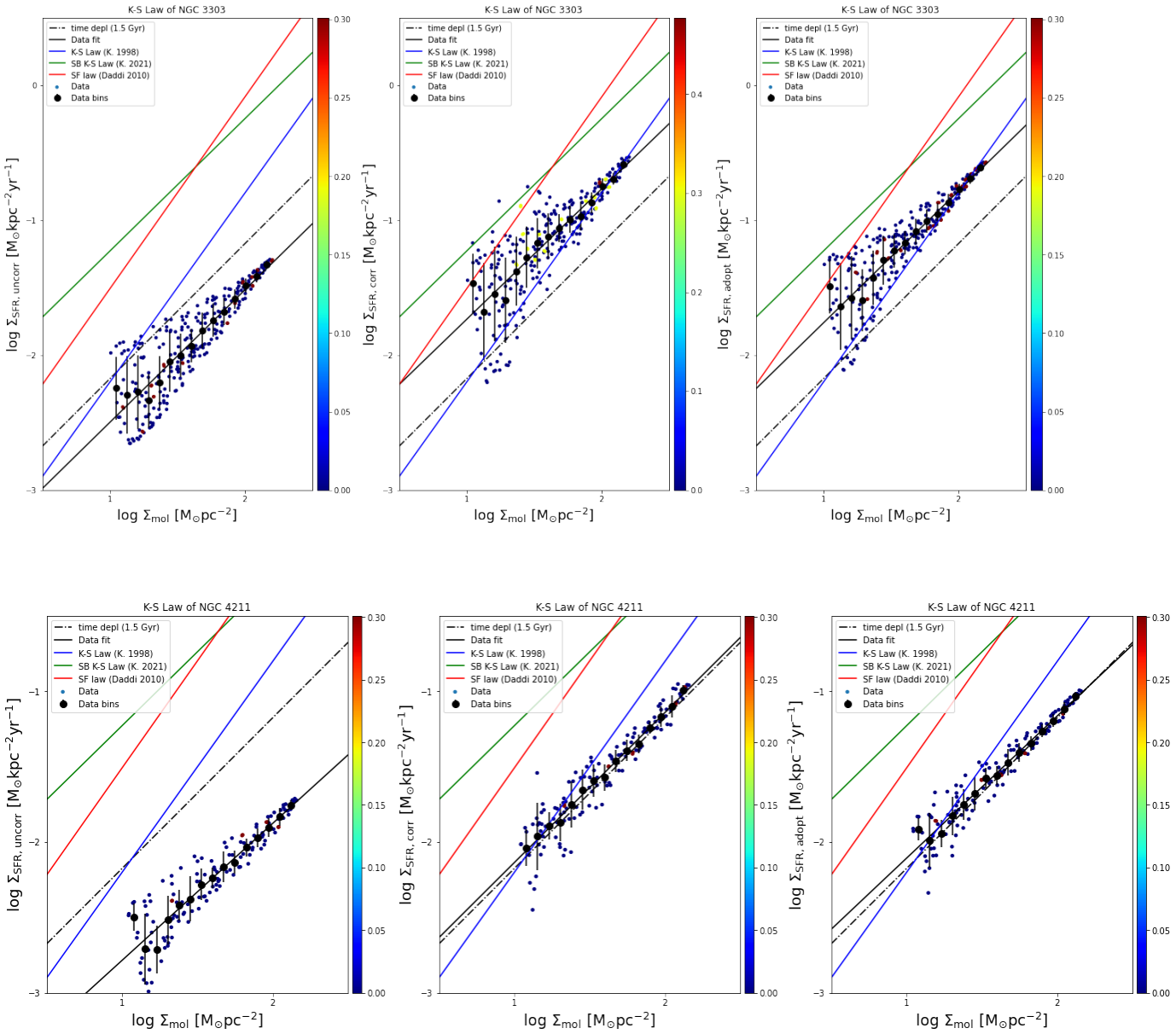

Figure 14: *Continuation*

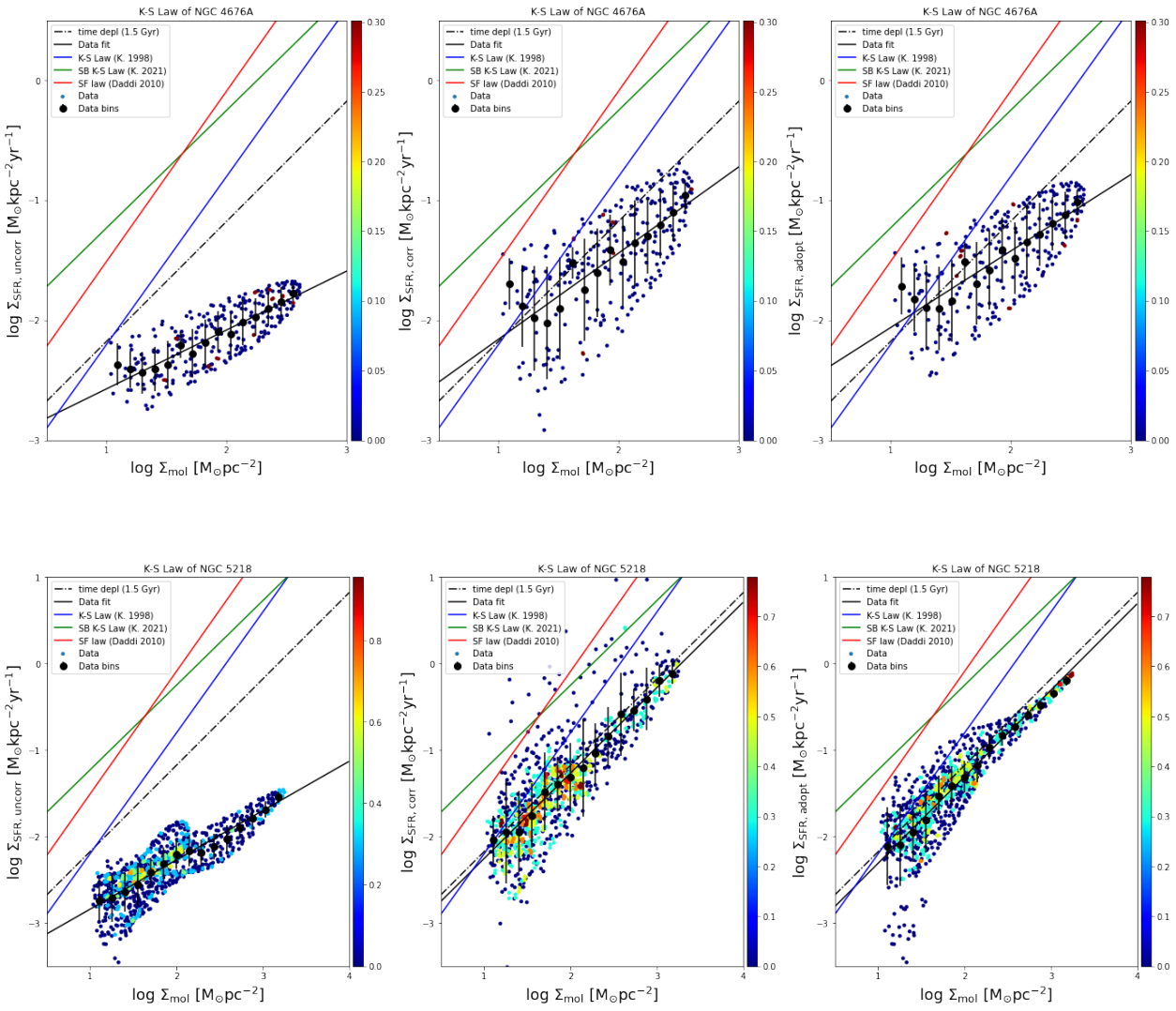

Figure 14: *Continuation*

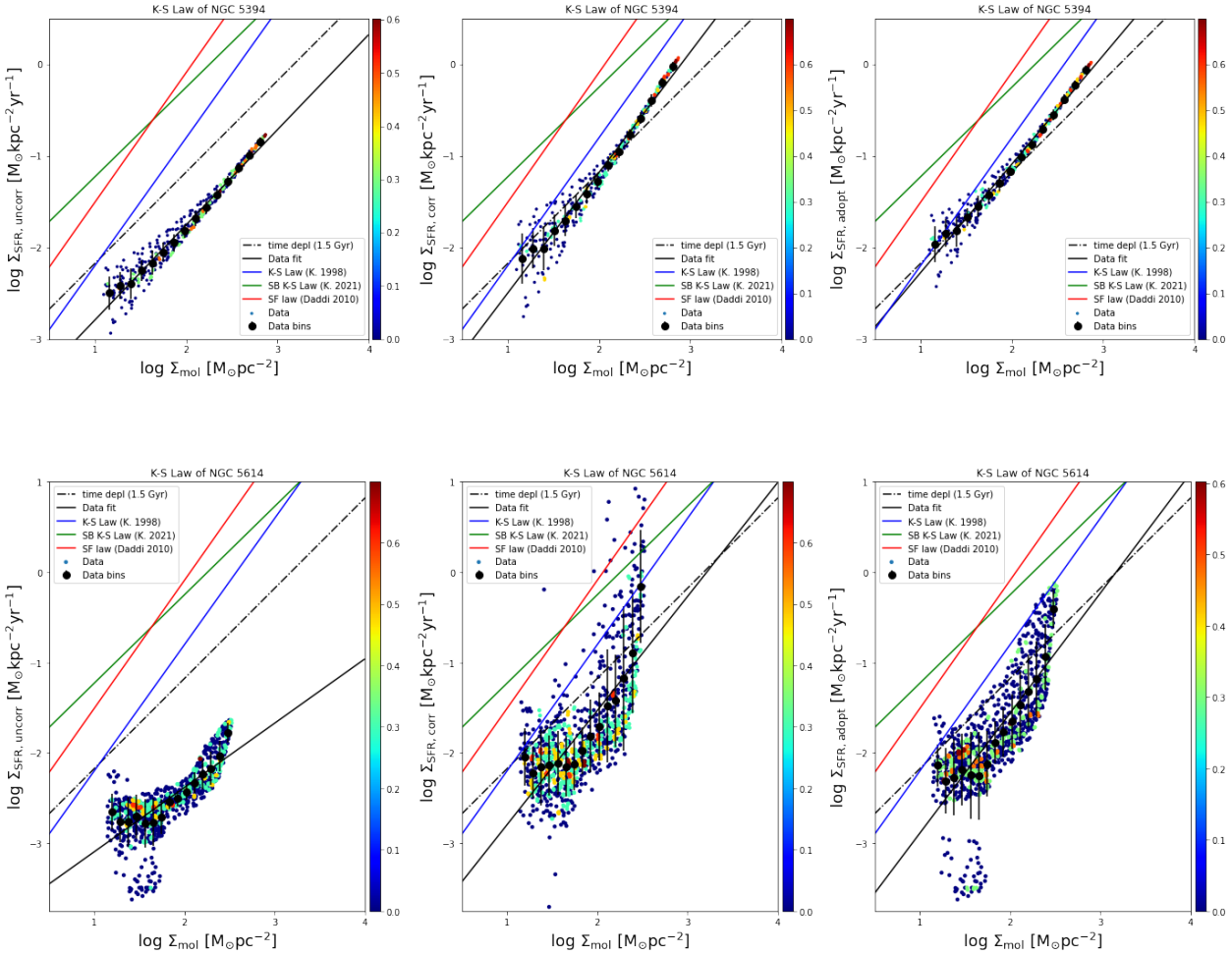

Figure 14: *Continuation*

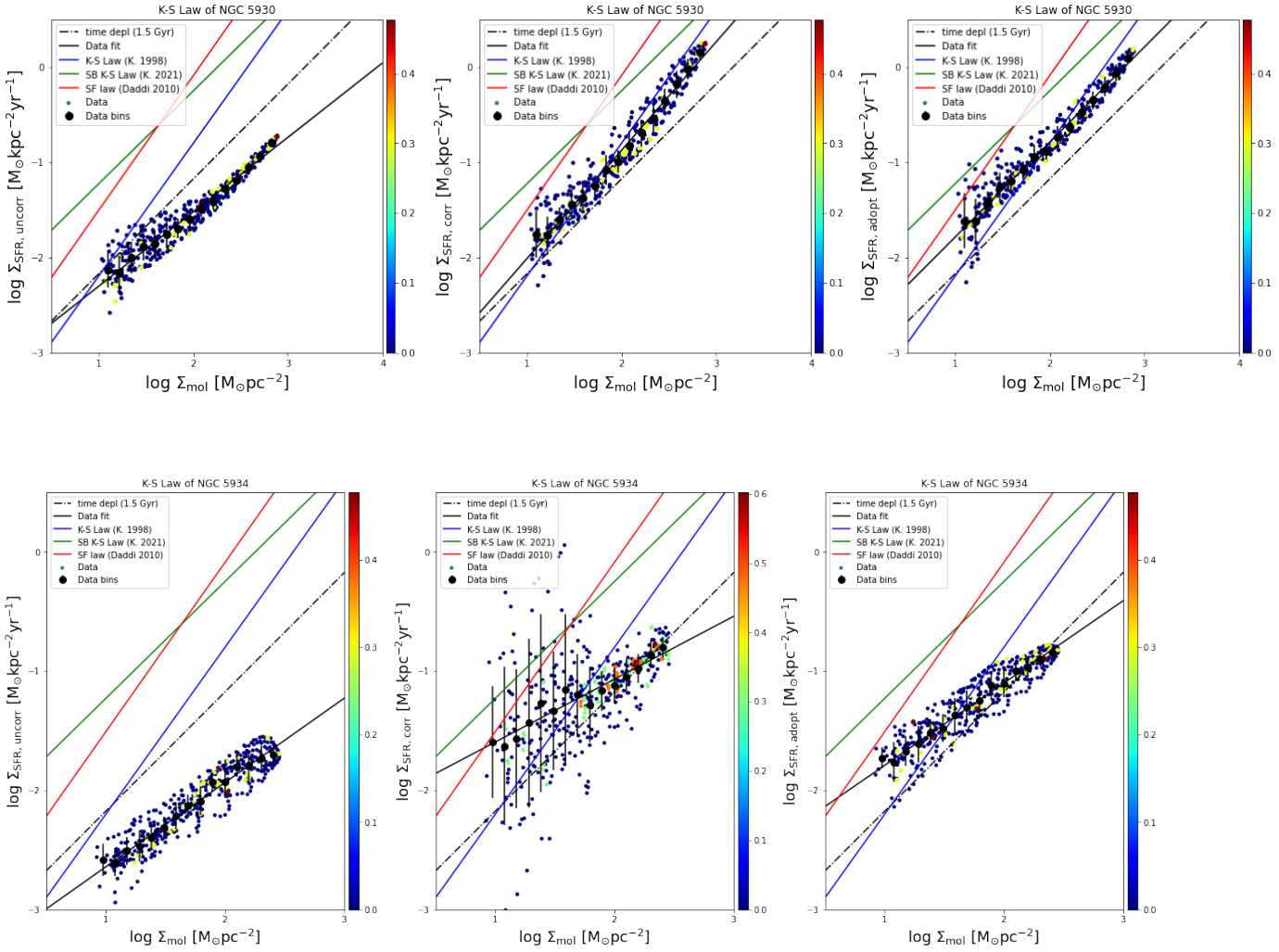

Figure 14: *Continuation*

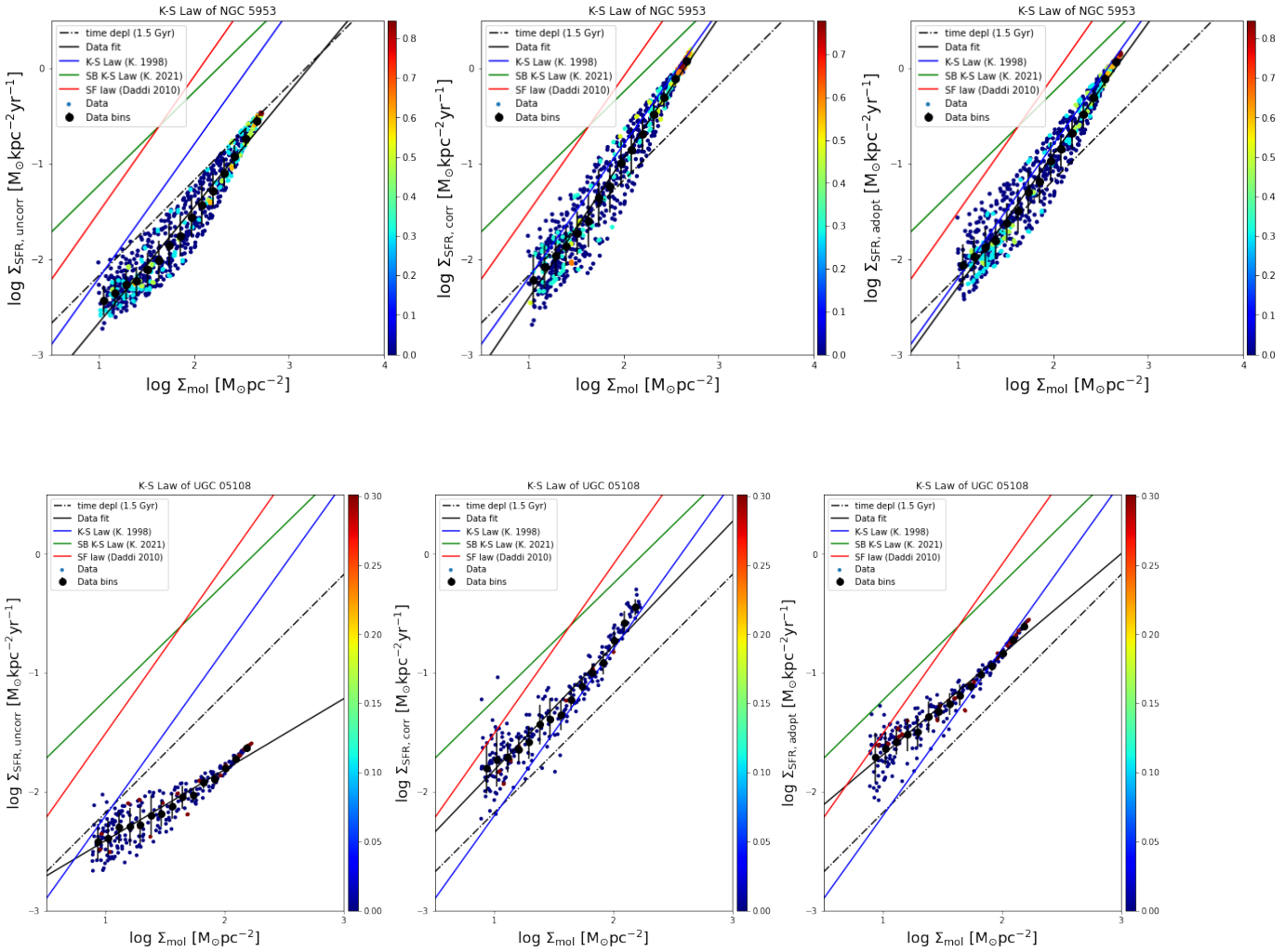

Figure 14: *Continuation*

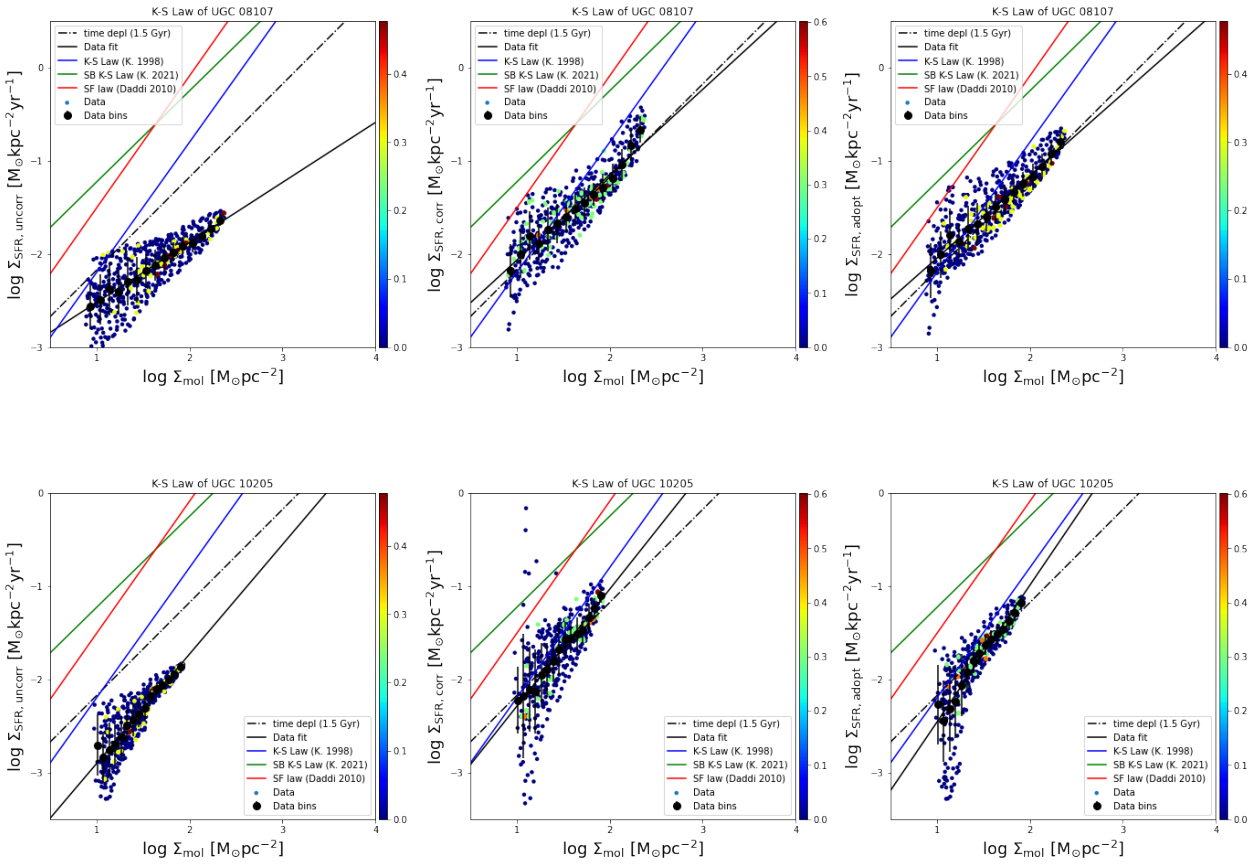

Figure 14: *Continuation*

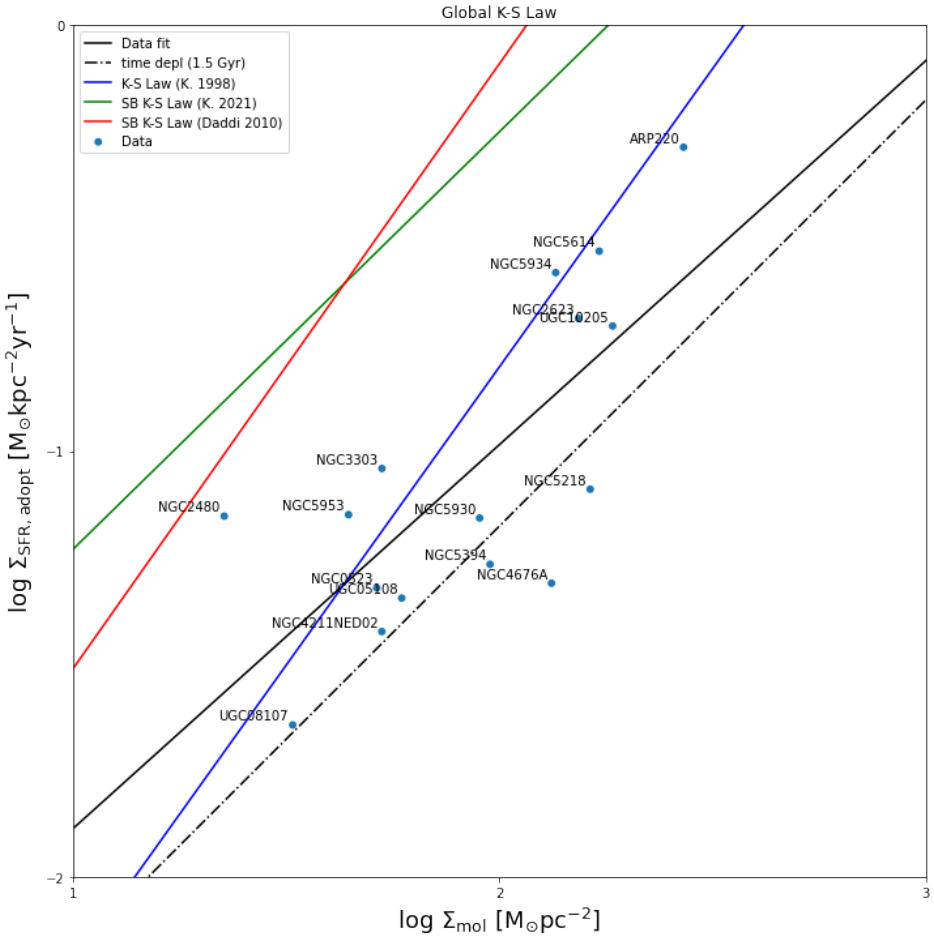

Figure 15: *Logarithmic Σ_{SFR}-Σ_{mol} relation, as known as Star Formation Law, of the entire sample. The black line is the best fit of the datasets, while the blue line is the best fit for normal spiral galxies from Kennicutt Jr (1998) and the green one is the is the best fir for starburst galaxies from Kennicutt and De Los Reyes (2021). The dash-point line indicates the time depletion of about 1.5 Gyr.*

In Figure 14 we show the local SF laws of each galaxies using the uncorrected, corrected and adapted SFR as well as the global SF law for whole the sample. We clearly see that the corrected and adapted SFR values are higher than the uncorrected ones because they were corrected from H_α extinction. Another aspect we can appreciate is that corrected SFR data points are more dispersed than the other 2. Therefore the SFR adapted data are the optimal ones because they were corrected form H_α extinction and the noise in it was reduced and for this the best results obtained are the ones derived by the adapted SFR data.

We binned their datasets in 15 databins using the function 'xy2binned' provided by the EDGE Python package. In each bin it is calculated the Σ_{SFR} mean values (represented as black filled points). The corresponding error bars are the total standard deviation derived from the calculus of the Σ_{SFR} mean values, and this error is bigger when the datapoints are scatter. We have plotted these databins to have a clearer vision of the trend of datapoints, specially for the plots where they are scatter, but to reproduce the SF law we have fitted only the datapoints. Most galaxies do not show much SFR values dispersion (to mention some of them: UGC 05108, NGC 5953, NGC 5930, NGC5394, NGC 4211 and NGC 2623), but we can appreciate 2 branches in NGC 2480, NGC 0523 and specially ARP 220. These SFR branches (high SFR and low SFR) are because the high and low SFEs regions that we saw before in Figure 9 for this 3 galaxies. That remarkable difference of SFE might be cause by the lack of HI in the regions with low SFE (Rownd and Young, 1999) since the SFR is proportional to the H_α luminosity produced in HI regions, as we see the brightess H_α zones in Figure 8. In the interacting-interacting galaxies the gas could have been dragged, maybe to the system mass center, leaving less atomic and molecular gas behind.

We also compare our SF laws (black lines) with others from the literature. To have a better comparison, we have plotted the SF laws from the literature assuming they share the same characteristic SFE of each galaxy. The SF laws obtained for each galaxy are summarized in the next table:

Name	**Uncorrected: logΣ_{SFR} =**	**Corrected: logΣ_{SFR} =**	**Adapted: logΣ_{SFR} =**
ARP 220	$(0.69 \pm 0.01)\Sigma_{mol}$ -3.76 $\pm$ 0.03	$(1.23 \pm 0.05)\Sigma_{mol}$ -2.99 $\pm$ 0.09	$(1.09 \pm 0.05)\Sigma_{mol}$ -3.61 $\pm$ 0.11
NGC 0523	$(0.69 \pm 0.03)\Sigma_{mol}$ -3.14 $\pm$ 0.05	$(0.52 \pm 0.05)\Sigma_{mol}$ -2.42 $\pm$ 0.09	$(0.63 \pm 0.05)\Sigma_{mol}$ -2.60 $\pm$ 0.08
NGC 2480	$(0.33 \pm 0.25)\Sigma_{mol}$ -2.20 $\pm$ 0.34	$(0.47 \pm 0.23)\Sigma_{mol}$ -2.04 $\pm$ 0.32	$(0.36 \pm 0.25)\Sigma_{mol}$ -1.93 $\pm$ 0.33
NGC 2623	$(0.70 \pm 0.01)\Sigma_{mol}$ -3.61 $\pm$ 0.02	$(1.38 \pm 0.03)\Sigma_{mol}$ -3.87 $\pm$ 0.06	$(1.20 \pm 0.02)\Sigma_{mol}$ -3.41 $\pm$ 0.04
NGC 3303	$(0.98 \pm 0.03)\Sigma_{mol}$ -3.48 $\pm$ 0.05	$(0.96 \pm 0.04)\Sigma_{mol}$ -2.70 $\pm$ 0.06	$(0.97 \pm 0.03)\Sigma_{mol}$ -2.73 $\pm$ 0.05
NGC 4211	$(0.90 \pm 0.03)\Sigma_{mol}$ -3.69 $\pm$ 0.05	$(0.99 \pm 0.03)\Sigma_{mol}$ -3.13 $\pm$ 0.04	$(0.94 \pm 0.02)\Sigma_{mol}$ -3.05 $\pm$ 0.04

Table 2: Summarize of SFR law fitting of each galaxy plotted in Figure 14 for the 3 different Σ_{SFR} values.

Name	Uncorrected: logΣ_{SFR} =	Corrected: logΣ_{SFR} =	Adapted: logΣ_{SFR} =
NGC 4676A	(0.49 ± 0.02)Σ_{mol} -3.06 ± 0.04	(0.71 ± 0.05)Σ_{mol} -2.87 ± 0.10	(0.63 ± 0.04)Σ_{mol} -2.70 ± 0.08
NGC 5218	(0.57 ± 0.01)Σ_{mol} -3.41 ± 0.02	(0.99 ± 0.02)Σ_{mol} -3.25 ± 0.04	(1.00 ± 0.01)Σ_{mol} -3.31 ± 0.03
NGC 5394	(1.04 ± 0.01)Σ_{mol} -3.84 ± 0.02	(1.31 ± 0.01)Σ_{mol} -3.82 ± 0.03	(1.18 ± 0.01)Σ_{mol} -3.47 ± 0.02
NGC 5614	(0.71 ± 0.02)Σ_{mol} -3.81 ± 0.03	(1.26 ± 0.04)Σ_{mol} -4.06 ± 0.08	(1.33 ± 0.03)Σ_{mol} -4.22 ± 0.06
NGC 5930	(0.78 ± 0.01)Σ_{mol} -3.09 ± 0.02	(1.14 ± 0.01)Σ_{mol} -3.16 ± 0.03	(1.00 ± 0.01)Σ_{mol} -2.80 ± 0.02
NGC 5934	(0.70 ± 0.01)Σ_{mol} -3.35 ± 0.02	(0.52 ± 0.05)Σ_{mol} -2.12 ± 0.09	(0.69 ± 0.01)Σ_{mol} -2.48 ± 0.02
NGC 5953	(1.21 ± 0.01)Σ_{mol} -3.88 ± 0.02	(1.47 ± 0.01)Σ_{mol} -3.89 ± 0.02	(1.38 ± 0.01)Σ_{mol} -3.68 ± 0.02
UGC 05108	(0.59 ± 0.01)Σ_{mol} -3.01 ± 0.02	(1.04 ± 0.02)Σ_{mol} -2.86 ± 0.03	(0.84 ± 0.01)Σ_{mol} -2.53 ± 0.02
UGC 08107	(0.64 ± 0.02)Σ_{mol} -3.17 ± 0.03	(0.91 ± 0.02)Σ_{mol} -2.99 ± 0.03	(0.88 ± 0.02)Σ_{mol} -2.93 ± 0.03
UGC 10205	(1.17 ± 0.03)Σ_{mol} -4.08 ± 0.04	(1.25 ± 0.06)Σ_{mol} -3.55 ± 0.09	(1.47 ± 0.05)Σ_{mol} -3.93 ± 0.07

Table 2: Continuation.

The Table 2 summarizes the SF laws for each galaxy and using the 3 Σ_{SFR} cases. Focusing on the results obtained from the adapted Σ_{SFR} datasets, since they make the best results, we can see that, in general, the slopes (the index n on 1) obtained from the data fittings are too different to the ones from the literature. In fact, the slope of the galaxies NGC 3303, NGC 4211, NGC 5218 and NGC 5930 coincide with SF law for starburst galaxies from Kennicutt and De Los Reyes (2021) (green line) with a n=0.98, while the slope of galaxies NGC 5953 and UGC 10205 are approximately equal to the ones obtained in Kennicutt Jr (1998) (blue line) and in Daddi et al. (2010) (red line).

The Figure 15 shows the local SF laws of each galaxies using the adapted Σ_{SFR}, since these values are corrected of H_α extinction and the noise was reduced. The value of Σ_{SFR} of each galaxy is the mean value of the Σ_{SFR} of all regions of these galaxies, as well as the Σ_{H_2}. We can see that the sample is divided in 2 groups: the first group (low Σ_{SFR}), formed by 11 galaxies, have a $-2 < log(\Sigma_{SFR}) < -1$ or a $0.01 < \Sigma_{SFR} < 0.1$, and the second one (high Σ_{SFR}), composed by 5 galaxies, have a $-1 < log(\Sigma_{SFR}) < 0$ or a $0.1 < \Sigma_{SFR} < 1$. This great difference between both groups are due to the high SFE of the galaxies from the second group. From the fitting we get a slope of $n = 0.90 \pm 0.22$ and a zeropoint of about $log(SFE) = -2.79 \pm 0.43$. We compare our results with the others from literature in the next table:

Work	n	$log(SFE[Myr^{-1}])$
This work	0.90 ± 0.22	-2.79 ± 0.43
Daddi et al. 2010	1.42	-2.93
Kennicutt 1998	1.40	-3.60
Kennicutt 2021	0.98	-2.21

Table 3: Results of the data fitting in this work comparing to the ones from the literature.

In Table 3 we put the fitting results (slope and zeropoint) obtained in Figure 15 and

compare them with the ones fro literature. We can see that the slope obtained is the smallest. The nearest one from it is the slope $n = 0.98$ from Kennicutt and De Los Reyes (2021) for LIRGs and starburst, but the slope $n = 1.42$ from Daddi et al. (2010) is also for starburst and is closer to the $n = 1.40$ from Kennicutt Jr (1998) for normal spiral galaxies. On the other hand, the logarithm of the SFE (zeropoint) obtained in this work is the second largest, only being smaller than the one from Kennicutt and De Los Reyes (2021). Also, the SFE from this work and the ones from Daddi et al. (2010) and Kennicutt and De Los Reyes (2021) are considerately bigger than the Kennicutt Jr (1998) SFE, this is what was expected because normal spiral galaxies have lower SFRs in comparison to the starburst ones.

5 Discussion

In this work we have studied the star formation of 16 interacting galaxies from the EDGE survey using the EDGE-Database which has the CO flux data obtained by observation with CARMA and H_α flux data from CALIFA. To do this, it has used the EDGE Python package (T. Wong et al. 2022, in preparation) in which we have elaborated the maps of Figure 10 and Figure 11 representing the correlation between the CO and H_α maps fluxes and the distribution of the SFE respectively for each galaxy. We have also plotted the SF law for each galaxy individually and for global scale case with the whole sample (Figure 14 and Figure 15) and compare them with the SF Law from the literature.

Analyzing the Figure 10 we find that there is a strong relation between the CO and H_α flux distribution on the galaxies. This affirmation gets stronger seeing the Figure 12 and Figure 13 (for the entire sample). Futhermore, in Figure 11 we see the distribution of the SFE in each galaxy, where in most of them the SFE is very high in many regions. This enhancement of the SFE leads to an increment on the SFR, which is an expected result since the SFR is triggered in pair-interacting galaxies (Knapen and Cisternas, 2015). However, in Figure 14 where we have plotted the SF law for each galaxy and compare it with ones from the literature, we can see that they do not get agree generally. From the fitting of the SF law, only the slope for the galaxies NGC 3303, NGC 4211NED02, NGC 5218 and NGC 5930 are too close to the one from Kennicutt and De Los Reyes (2021) (with a slope $n = 0.98 \pm 0.08$) obtained using a sample of 83 LIRGs), while the slope for the galaxies NGC 5953 and UGC 10205 are too similar to the ones from Kennicutt Jr (1998) and Daddi et al. (2010) for starburst or SB galaxies with slopes of $n = 1.40$ and $n = 1.42$ respectively. But for the rest of the sample it has slopes that differ a lot from the ones of the literature. Something similar happens in the global (Figure 15) case when we have tried to fit the slope of the SF law for the whole sample, finding that it is smaller than others, with a value of $n = 0.90 \pm 0.22$, only coinciding with the one from Kennicutt and De Los Reyes (2021) if we take into account the slope error. This mismatch seems to occurs to SB galaxies because in Daddi et al. (2010), the SB galaxy sample have the same slope as the normal spiral galaxy sample from that work but it is shifted to the left on the Σ_{mol} axis , having 2 SF laws. Also in Kennicutt and De Los Reyes (2021) for the SB sample it has a different slope to the one

obtained from the normal spiral galaxy sample.

The comparison between the results of the SF law obtained in this work and the ones from the literature reinforce the idea that its nature is bimodal, talked in many works like Kennicutt and De Los Reyes (2021), Daddi et al. (2010) and Genzel et al. (2010) saying that the CO-to-H_2 conversion factor might be lower in SB galaxies than in the normal spiral galaxy sequence. In the simulation made in Bournaud et al. (2015) they found that the CO-toH_2 conversion factor (or α_{CO}) is too sensible to changes in the ISM. The turbulence on the ISM of pair-interacting galaxies is larger than spiral galaxies, compressing the gas making denser gas regions and consequently triggering the star formation within them. However, more than the turbulence is the velocity gradient that drives the line width of CO which are higher in the densest gas regions where the SFR is larger and the α_{CO} is smaller. Also we find the same explanation in Narayanan et al. (2011): the α_{CO} depends on the physical conditions of the ISM, overall by turbulance and gas temperature within the densest regions, leading the drop of α_{CO} in them, other than it also depends on the mereger strength.

6 Conclusion.

In base on the analysis and discussion we have done, we come to the following conclusions:

- Most of the galaxies have a relative high SFE. This is expected because merger galaxies have an little enhancement on the SFE respect to the normal spirals galaxies. This increment on the SFE is due the compression and shocks of the gas, rising its density in some regions due to turbulence cause by the interaction of galaxies, increasing the SFR there (Dopita et al., 2002).
- The regions where the H_α flux emission is the highest correspond to the brightest regions in CO flux (specially near the nucleus) as we saw in Figure 10). Also, we verified the strong relation between the logarithm H_α flux and the logaritm CO flux. This relation is a form to express the SF law since the SFR is derived from the H_α flux Rosa-González et al. (2002) and the molecular mass of the giant molecular clouds is calculated by its CO flux Bolatto et al. (2013).
- The SF law of the sample obtained is different to the ones from literature because in merger galaxies (that they are usually starburst galaxies), the ISM experiments changes in its physical properties. Those changes, specially in the turbulence and velocity gradient, drop the α_{CO}, which is also dependent on the strength of the mergers.

References

A. J. Beasley and S. N. Vogel. Carma: specifications and status. In *Millimeter and Submillimeter Detectors for Astronomy*, volume 4855, pages 254–264. SPIE, 2003.

E. A. Bergin and M. Tafalla. Cold dark clouds: the initial conditions for star formation. *arXiv preprint arXiv:0705.3765*, 2007.

A. D. Bolatto, M. Wolfire, and A. K. Leroy. The co-to-h2 conversion factor. *arXiv preprint arXiv:1301.3498*, 2013.

A. D. Bolatto, T. Wong, D. Utomo, L. Blitz, S. N. Vogel, S. F. Sánchez, J. Barrera-Ballesteros, Y. Cao, D. Colombo, H. Dannerbauer, R. García-Benito, R. Herrera-Camus, B. Husemann, V. Kalinova, A. K. Leroy, G. Leung, R. C. Levy, D. Mast, E. Ostriker, E. Rosolowsky, K. M. Sandstrom, P. Teuben, G. van de Ven, and F. Walter. The EDGE-CALIFA survey: Interferometric observations of 126 galaxies with CARMA. *The Astrophysical Journal*, 846(2):159, sep 2017. doi: 10.3847/1538-4357/aa86aa. URL https://doi.org/10.3847%2F1538-4357%2Faa86aa.

F. Bournaud, E. Daddi, A. Weiß, F. Renaud, C. Mastropietro, and R. Teyssier. Modeling co emission from hydrodynamic simulations of nearby spirals, starbursting mergers, and high-redshift galaxies. *Astronomy & Astrophysics*, 575:A56, 2015.

C. R. Bridge, R. G. Carlberg, and M. Sullivan. The cfhtls-deep catalog of interacting galaxies. i. merger rate evolution to z= 1.2. *The Astrophysical Journal*, 709(2):1067, 2010.

C. Catalán-Torrecilla, A. G. De Paz, A. Castillo-Morales, J. Iglesias-Páramo, S. F. Sánchez, R. Kennicutt, P. G. Pérez-González, R. Marino, C. Walcher, B. Husemann, et al. Star formation in the local universe from the califa sample-i. calibrating the sfr using integral field spectroscopy data. *Astronomy & Astrophysics*, 584:A87, 2015.

A. Cimatti, F. Fraternali, and C. Nipoti. *Introduction to Galaxy Formation and Evolution: From Primordial Gas to Present-Day Galaxies*. Cambridge University Press, 2019.

C. J. Conselice, M. A. Bershady, and J. S. Gallagher. Physical morphology and triggers of starburst galaxies. *arXiv preprint astro-ph/0001195*, 2000.

E. Daddi, D. Elbaz, F. Walter, F. Bournaud, F. Salmi, C. Carilli, H. Dannerbauer, M. Dickinson, P. Monaco, and D. Riechers. Different star formation laws for disks versus starbursts at low and high redshifts. *The Astrophysical journal letters*, 714(1):L118, 2010.

I. De Looze, D. Cormier, V. Lebouteiller, S. Madden, M. Baes, G. J. Bendo, M. Boquien, A. Boselli, D. L. Clements, L. Cortese, et al. The applicability of far-infrared fine-structure lines as star formation rate tracers over wide ranges of metallicities and galaxy types. *Astronomy & Astrophysics*, 568:A62, 2014.

M. Dopita, M. Pereira, L. Kewley, and M. Capaccioli. Star formation rates in interacting starburst galaxies. *The Astrophysical Journal Supplement Series*, 143(1):47, 2002.

R. S. Ellis. The formation and evolution of galaxies. *arXiv preprint astro-ph/9807287*, 1998.

N. J. Evans. Physical conditions in regions of star formation. *arXiv preprint astro-ph/9905050*, 1999.

R. Genzel, L. Tacconi, J. Gracia-Carpio, A. Sternberg, M. Cooper, K. Shapiro, A. Bolatto, N. Bouché, F. Bournaud, A. Burkert, et al. A study of the gas–star formation relation over cosmic time. *Monthly notices of the royal astronomical Society*, 407(4):2091–2108, 2010.

P. Girichidis, C. Federrath, R. Banerjee, and R. S. Klessen. Importance of the initial conditions for star formation–i. cloud evolution and morphology. *Monthly Notices of the Royal Astronomical Society*, 413(4):2741–2759, 2011.

S. Glover and M.-M. M. Low. On the relationship between molecular hydrogen and carbon monoxide abundances in molecular clouds. *Monthly Notices of the Royal Astronomical Society*, 412(1):337–350, 2011.

A. M. Hopkins, A. Connolly, D. Haarsma, and L. Cram. Toward a resolution of the discrepancy between different estimators of star formation rate. *The Astronomical Journal*, 122 (1):288, 2001.

H. Hwang, D. Elbaz, M. Dickinson, V. Charmandaris, E. Daddi, D. Le Borgne, V. Buat, G. Magdis, B. Altieri, H. Aussel, et al. Goods-herschel: the impact of galaxy-galaxy interactions on the far-infrared properties of galaxies. *Astronomy & Astrophysics*, 535: A60, 2011.

S. Jogee, S. H. Miller, K. Penner, R. E. Skelton, C. J. Conselice, R. S. Somerville, E. F. Bell, X. Z. Zheng, H.-W. Rix, A. R. Robaina, et al. History of galaxy interactions and their impact on star formation over the last 7 gyr from gems. *The Astrophysical Journal*, 697 (2):1971, 2009.

R. Joseph and G. Wright. Recent star formation in interacting galaxies–ii. super starbursts in merging galaxies. *Monthly Notices of the Royal Astronomical Society*, 214(2):87–95, 1985.

A. Kelz, M. A. Verheijen, M. M. Roth, S. M. Bauer, T. Becker, J. Paschke, E. Popow, S. F. Sánchez, and U. Laux. Pmas: The potsdam multi-aperture spectrophotometer. ii. the wide integral field unit ppak. *Publications of the Astronomical Society of the Pacific*, 118(839): 129, 2006.

R. C. Kennicutt and M. A. De Los Reyes. Revisiting the integrated star formation law. ii. starbursts and the combined global schmidt law. *The Astrophysical Journal*, 908(1):61, 2021.

R. C. Kennicutt Jr. The global schmidt law in star-forming galaxies. *The astrophysical journal*, 498(2):541, 1998.

J. H. Knapen and M. Cisternas. Starbursts are preferentially interacting: Confirmation from the nearest galaxies. *The Astrophysical Journal Letters*, 807(1):L16, 2015.

M. R. Krumholz and C. F. McKee. A general theory of turbulence-regulated star formation, from spirals to ultraluminous infrared galaxies. *The astrophysical journal*, 630(1):250, 2005.

D. Narayanan, M. Krumholz, E. C. Ostriker, and L. Hernquist. The co–h2 conversion factor in disc galaxies and mergers. *Monthly Notices of the Royal Astronomical Society*, 418(1): 664–679, 2011.

M. W. Pound, R. Hobbs, and S. Scott. The carma data viewer. In *Astronomical Data Analysis Software and Systems X*, volume 238, page 82, 2001.

D. Puy and M. Signore. Primordial molecular clouds. In *AIP Conference Proceedings*, volume 476, pages 105–116. American Institute of Physics, 1999.

D. Rosa-González, E. Terlevich, and R. Terlevich. An empirical calibration of star formation rate estimators. *Monthly Notices of the Royal Astronomical Society*, 332(2):283–295, 2002.

M. M. Roth, A. Kelz, T. Fechner, T. Hahn, S.-M. Bauer, T. Becker, P. Böhm, L. Christensen, F. Dionies, J. Paschke, et al. Pmas: The potsdam multi-aperture spectrophotometer. i. design, manufacture, and performance. *Publications of the Astronomical Society of the Pacific*, 117(832):620, 2005.

B. K. Rownd and J. S. Young. The star formation efficiency within galaxies. *The Astronomical Journal*, 118(2):670, 1999.

D. S. Rupke, L. J. Kewley, and J. E. Barnes. Galaxy mergers and the mass–metallicity relation: evidence for nuclear metal dilution and flattened gradients from numerical simulations. *The Astrophysical Journal Letters*, 710(2):L156, 2010.

S. Sánchez, R. Kennicutt, A. G. De Paz, G. Van de Ven, J. Vílchez, L. Wisotzki, C. Walcher, D. Mast, J. Aguerri, S. Albiol-Pérez, et al. Califa, the calar alto legacy integral field area survey-i. survey presentation. *Astronomy & Astrophysics*, 538:A8, 2012.

P. Torrey, T. J. Cox, L. Kewley, and L. Hernquist. The metallicity evolution of interacting galaxies. *The Astrophysical Journal*, 746(1):108, 2012.

C. Walcher, L. Wisotzki, S. Bekeraité, B. Husemann, J. Iglesias-Páramo, N. Backsmann, J. B. Ballesteros, C. Catalán-Torrecilla, C. Cortijo, A. del Olmo, et al. Califa: a diameter-selected sample for an integral field spectroscopy galaxy survey. *Astronomy & Astrophysics*, 569:A1, 2014.

D. P. Woody, A. J. Beasley, A. D. Bolatto, J. E. Carlstrom, A. Harris, D. W. Hawkins, J. Lamb, L. Looney, L. G. Mundy, R. L. Plambeck, et al. Carma: a new heterogeneous millimeter-wave interferometer. In *Millimeter and Submillimeter Detectors for Astronomy II*, volume 5498, pages 30–41. SPIE, 2004.